Simulating the Core Collapse of Self-Interacting Dark Matter Halos

Kai Ulrich

Bachelor's Thesis

Institut für Theoretische Physik
Fachbereich Physik
Goethe-Universität Frankfurt am Main

Betreuerin: Prof. Dr. Laura Sagunski
Zweitgutachter: Dr. Moritz Fischer
Eingereicht am 17.11.2025

Abstract

The gravothermal collapse of self-interacting dark matter (SIDM) halos can produce intermediate-mass black holes and alleviate some of the tension around the formation of supermassive black holes observable today. The goal of this work is to find a general calibration for the gravothermal fluid model, which can correctly simulate the core collapse of different SIDM halos. This method would enable the description of the evolution for the halo without the need for an expensive N-body simulation. For calibrating the gravothermal fluid code, three halos are simulated for different values of the calibration constant as well as the scaling of the heat conductivity. This is then compared to an N-body simulation and another method called KiSS-SIDM. The results of this comparison indicate that using these two parameters, the simulation results of KiSS-SIDM can be somewhat matched in accuracy, but with both of these methods still having some problems at describing parts of the evolution of these halos.

Zusammenfassung

Der gravothermale Kollaps von Halos aus selbst-wechselwirkender dunkler Materie (SIDM) kann schwarze Löcher von mittlerer Masse erzeugen und somit möglicherweise Probleme in der Entstehungsgeschichte von supermassiven schwarzen Löchern lösen. Diese Arbeit dient dem Kalibrieren des Gravothermal Fluid Models zum Simulieren des Kernkollapses von verschiedenen selbst-wechselwirkenden dunkle Materie Halos. Durch diese Methode ist es möglich, die Evolution des Halos zu beschreiben, wofür sonst teure N-body Simulationen gebraucht werden. Für die Kalibrierung des Gravothermal Fluid Models werden drei Halos für unterschiedliche Kalibrierungskonstanten sowie Skalierungen bei der Wärmeleitung simuliert. Die Ergebnisse deuten darauf hin, dass unter Verwendung dieser beiden Parameter die Genauigkeit einigermaßen mit den der KiSS-SIDM Simulationsergebnisse übereinstimmen, aber beide Methoden noch Probleme bei der Beschreibung von Teilen der Evolution dieser Halos haben.

Contents

1. Introduction **1**

2. Theory **2**

2.1. Cosmology . . . 2

2.1.1. Inflation . . . 2

2.1.2. Dark Energy . . . 4

2.1.3. Dark Matter . . . 4

2.1.4. Missing Satellites Problem . . . 4

2.1.5. Core-Cusp Problem . . . 6

2.2. SIDM . . . 7

2.3. Evolution of SIDM Halos . . . 7

3. Simulation Methods **8**

3.1. The Gravothermal Fluid Model . . . 8

3.1.1. Mass Conservation . . . 8

3.1.2. Hydrostatic Equilibrium . . . 9

3.1.3. Heat Transfer . . . 10

3.1.4. SIDM Gravothermal Fluid . . . 11

3.1.5. Numerical Implementation . . . 12

3.2. Other Methods . . . 14

3.2.1. KiSS-SIDM . . . 14

3.2.2. N-body . . . 15

4. Setup **17**

4.1. Gravothermal Fluid Initial Parameters . . . 18

5. Results **19**

5.1. First Halo . . . 19

5.2. Second Halo . . . 21

5.3. Third Halo . . . 23

5.4. Changing the Thermal Conductivity . . . 25

6. Conclusions **30**

A. List of Parameters used for the Gravothermal Fluid Code Runs **32**

B. Error for Gravothermal Fluid Code **32**

References **35**

1. Introduction

The goal of cosmology is to model the evolution of the universe. This entails the need for accurate predictions of the very beginning, starting with quantum fluctuations, the so-called 'Seeds of Structure', up to the present, where these seeds developed into all structures observable today [1]. Currently, the ΛCDM cosmological model is one of the best at describing the whole evolution of our universe and is in good agreement with a wide range of observations, including large-scale structures, the anisotropy of the cosmic microwave background (CMB) and the light element abundance [2]. However, it also has some problems, where the model's predictions do not match our current measurements. Some difficulties of the theory matching observations, like the core-cusp problem [3] or the missing satellite problem [4], led to the proposal of self-interactions between dark matter particles (SIDM) [5]. The gravothermal core collapse of SIDM halos could also help to explain the occurrence of high redshift supermassive black holes [6] and modeling the collapse of these halos could prove to be helpful at finding limits for the interaction cross-section of SIDM. Today this is mostly done via N-body simulations, which are computational expensive. Thus finding other methods, which are faster and less expensive but can accurately simulate the halos evolution and core collapse, is an open field of research and scientific debate.

The aim of this work is to compare the gravothermal fluid approach for simulating SIDM halos to an N-body simulation and a method called KiSS-SIDM. It starts with a short overview on why SIDM is interesting to consider (Section 2), explains and derives the gravothermal fluid method and gives a short overview on how the N-body simulation and KiSS-SIDM work (Section 3). The initial conditions for the three halos are detailed in Section 4, followed by the results of the simulations (Section 5) and the conclusion from the comparison of the three different methods (Section 6).

2. Theory

2.1. Cosmology

Only six parameters are needed to characterize the ΛCDM model, with the latest values coming from the final Planck measurements [7]. These parameters are

- Baryon density: $\omega_b = 0.022\,33(15)$
- Cold dark matter density: $\omega_c = 0.1198(12)$
- Approximation of the sound horizon at recombination (Θ_{MC}): $100\Theta_{MC} = 1.040\,89(31)$
- Reionization optical depth: $\tau = 0.0540(140)$
- Amplitude of curvature perturbations (A_s): $\ln(10^{10}A_s) = 3.043(14)$
- Primordial spectral index: $n_s = 0.9652(42)$

Although ΛCDM is successful at explaining many important things concerning the structure and evolution of our universe [2], like the temperature fluctuations of the cosmic microwave background seen in Figure 1, there are three important aspects of it which involve physics outside the standard model of particle physics. Two of these are incorporated into the name ΛCDM. The first one being dark-energy, represented by the Λ for Einstein's cosmological constant, while CDM is the abbreviation for cold dark matter. The third one is inflation [2].
The following passages will give a short overview on why these additions to the Big Bang model are needed to account for phenomena observed in the present universe.

2.1.1. Inflation

One of the shortcomings of the Big Bang model is encapsulated in the Horizon Problem. It concerns the isotropy of the Cosmic Microwave Background (CMB) observed today which is in contradiction with the fact that the CMB should, according to the Big Bang model, consist of roughly 10^5 causally disconnected regions [8]. This would have made the development of a thermal equilibrium and therefor our observations of an almost uniform CMB temperature impossible. This problem can be resolved through the introduction of inflation by postulating that this thermal equilibrium is a remnant of a once fully causally connected universe, before it entered into a phase of exponential expansion [8].

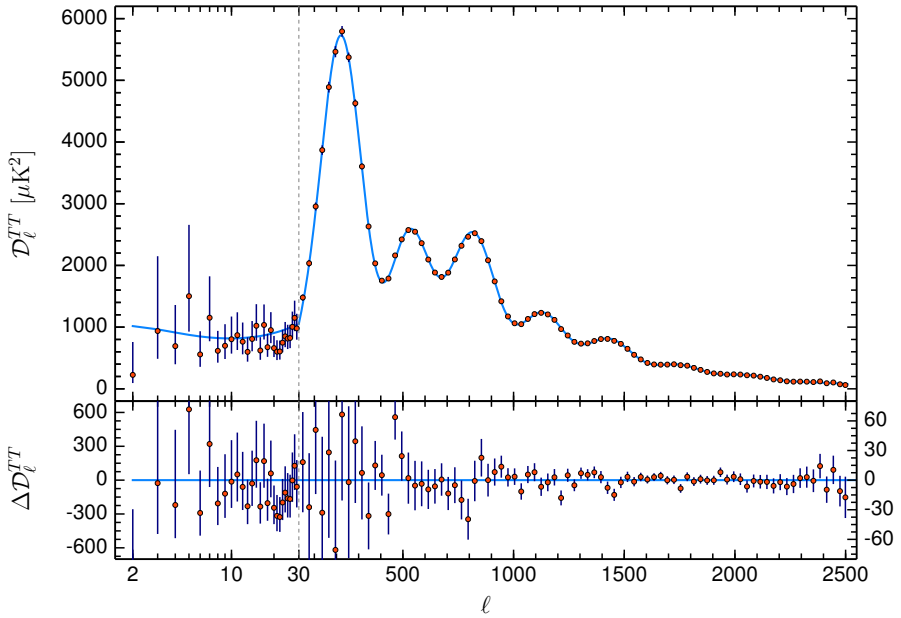

Figure 1: In the upper panel the multipole moment l, which corresponds to the angular scale, is plotted against the temperature fluctuations of the cosmic microwave background and fits (blue line) the prediction from the ΛCDM model to it. The lower panel shows the deviations of the measurements from the model (residuals). This figure is reprinted from Figure 1 of Ref. [7]

2.1.2. Dark Energy

An accelerated expansion was introduced to explain the age of the universe implied by some globular clusters [9], as well as the observations of high-redshift supernovae [10] with an observed distance greater than what was expected for a matter-only Universe. For this, the cosmological constant Λ was reinstated in the ΛCDM model representing dark energy with an equation of state $w = -1$.

2.1.3. Dark Matter

With his discovery in 1933, that the visible matter in galaxy clusters is not sufficient to hold them together, Fritz Zwicky proposed the existence of cold dark matter (CDM) [11]. The first theory for this cold and only gravitationally interacting non-baryonic matter was proposed in 1982 by James Peebles [12] and later refined by Blumenthal et al. [13]. Today, the discrepancy between the matter density $\omega_m \approx 0.14$ and the baryon density $\omega_b \approx 0.02$ [7], is strong evidence for the existence of CDM [2]. Its density is measured at $\omega_c \approx 0.12$ [7].
At the moment there is much research being conducted on CDM with many theories concerning its nature and possible means of detection, be it direct or indirect, as well as its production using accelerators. But there are some problems with the description of CDM in ΛCDM, of which two are the Core-Cusp problem and the Missing Satellites problem.

2.1.4. Missing Satellites Problem

In 1993, Kauffman et al. found a discrepancy between the estimated number of DM sub-halos and the observed number of satellite galaxies [14]. This problem got more pressing as more accurate simulations found the same phenomenon [4][15], which can be seen in Figure 2. Although in recent years there seems to be an increase in newly discovered Milky Way satellites [16], there still remains a discrepancy between the predictions of some models and observations [17]. But if this problem persists, accounting for starless sub-halos [17] or reducing the number of satellites in simulations by properly including baryons, which was already shown to work to some extent in Ref. [18], could help to alleviate it.

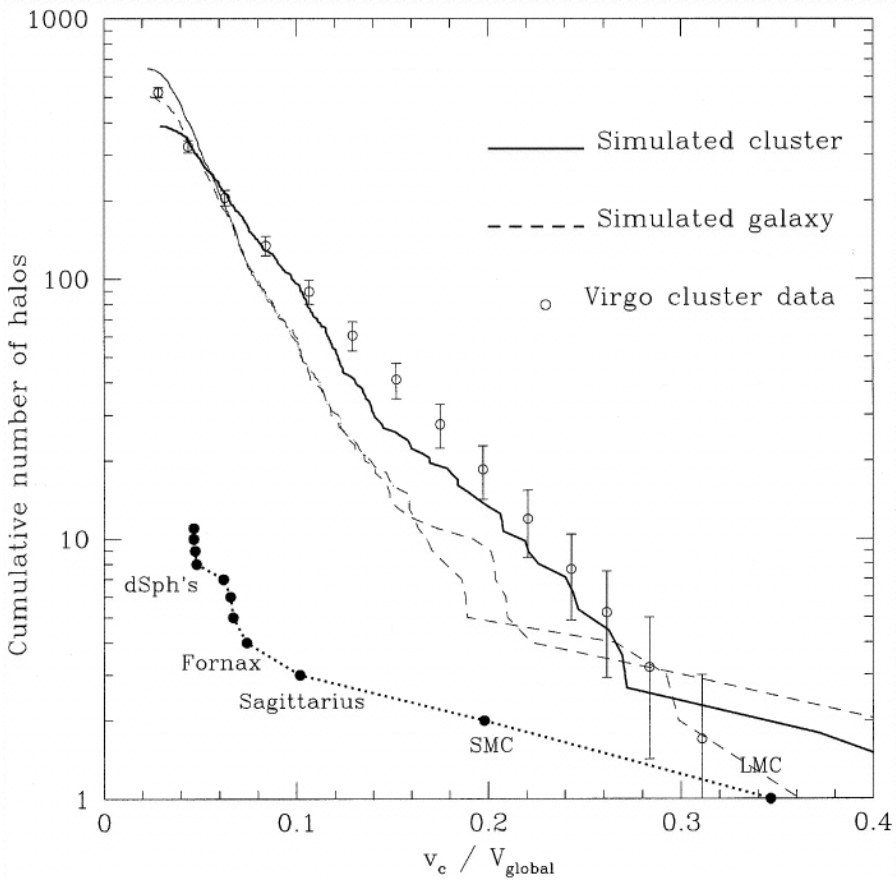

Figure 2: Here, the number of sub-halos is plotted against their circular velocity v_c normalized by the circular velocity V_{global} of the halo they inhabit. This is done for the Milky Way and the Virgo cluster, where there are included measurements for both represented by the dots, and the corresponding simulation results with the dashed lines for galactic sized halos and the solid line for a cluster halo. There is a difference of roughly a factor of 50 between the simulated number of satellites larger than the dSph and the observed number. This figure is reprinted from Figure 2 of Ref. [15]

2.1.5. Core-Cusp Problem

In the 1980s, observations indicated that (gas-rich, late-type) dwarf and disk galaxies have dark matter distributions with a cored central region of almost constant DM density [3]. With the emergence of numerical N-body simulations for CDM, Navarro et al. described in Ref. [19] an 'universal density profile' for DM halos, which is known as the Navarro-Frank-White profile

$$\rho_{\mathrm{NFW}}(r) = \frac{\rho_s}{\frac{r}{r_s}\left(1+\frac{r}{r_s}\right)^2} \,. \tag{1}$$

Navarro et al. and others found that simulations of halos based on CDM result in a cusp like ($\rho \propto r^{-1}$) central DM distribution. The difference between these two profiles can be seen in Figure 3. With high-resolution velocity fields many of the possible observational or physical systematic effects regarding the measurements had their potential impact significantly reduced [3]. This let to the formulation of the core-cusp problem, which tackles the discrepancy between the observations and simulations. Possible solutions are baryonic effects or alterations to the DM model, like introducing interactions between the DM particles, which will be shown in the next subsection.

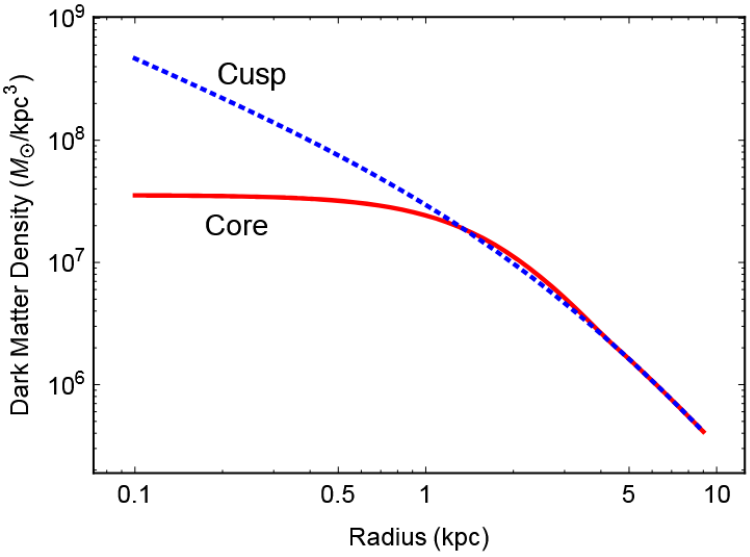

Figure 3: The different density profiles for the central halo regions. The blue dotted line represent the cuspy NFW profile, while the red solid line shows the cored profile favored by observations and recreated using SIDM simulations. This figure was reprinted from Figure 4 (right panel) of Ref. [20]

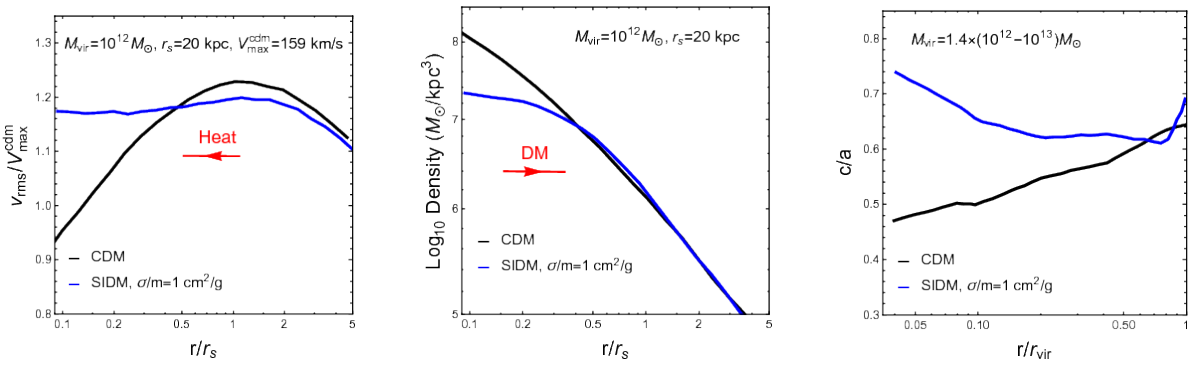

(a) (b) (c)

Figure 4: Velocity and density profiles as well as the ratio between the minor and major axis for a CDM and SIDM halo. This figure is reprinted from Figure 2 of Ref. [20].

2.2. SIDM

By introducing the possibility for the DM particles to scatter elastically via 2-body interactions, Spergel and Steinhardt [5] tried to solve the problems CDM has at describing small scales. This change to the inner workings of DM has a great effect on the makeup of DM-Halos. The isothermal velocity dispersion is almost constant for SIDM halos, while decreasing near the center for CDM (see Figure 4a). This is because the self interactions make heat transfer possible, heating up the central regions. It also creates a cored density profile, in contrast to the cuspy profile of CDM, which can be seen in Figure 4b, and leads to more spherical halos, seen in Figure 4c, where the ratio between the minor to the major axis is closer to 1 for the SIDM case. While SIDM halos are less concentrated and therefore at greater risk of tidal stripping or evaporation due to ram pressure, which would lead to fewer satellites, these effects can be neglected, as the upper bound for the cross-section per unit mass $\sigma_m \approx 1.00\,\mathrm{cm}^2\,\mathrm{g}^{-1}$ [20] favored at the moment [21], [22] is too low for them to be relevant. Most models today also take it to be at least slightly velocity dependent [20].

2.3. Evolution of SIDM Halos

Assuming an initial NFW profile for an isolated SIDM halo with an interaction cross-section per mass $\sigma_m = 5.00\,\mathrm{cm}^2\,\mathrm{g}^{-1}$, its evolution, as described in Ref. [23], is the following:

The early stages are characterized by a long mean free path (LMFP, the mean free path is longer than the Jeans length) dominated heat transfer. Equalizing velocities in the central regions, caused by the self-interactions of the dark matter particles lead to an increasing core temperature, which results in an expanding core with constant density. The now isothermal core has reached the point in its evolution, where the central density is at its minimum. This is followed by the core collapse, with the central density greatly increasing. This continues until the thermal conductivity for the short mean free path (SMFP, the mean free path is shorter than the Jeans length) κ_{SMFP} is greater or equal to the one for the LMFP κ_{LMFP}

$$\kappa_{\mathrm{SMFP}} \geq \kappa_{\mathrm{LMFP}} \ , \tag{2}$$

in the core, which indicates the start of the SMFP core collapse. Thus, the now optically thick core's density and temperature start increasing faster. The evolution of the halo ends with reaching the relativistic instability and the formation of a black hole.

3. Simulation Methods

3.1. The Gravothermal Fluid Model

A computational less taxing method, compared to N-body simulations, to model SIDM halos is the gravothermal fluid model, in which DM is a thermally conducting fluid in quasistatic virial equilibrium and the halo is isotropic and spherical with a density $\rho(r,t)$ and mass profile $M(r,t)$. The gravothermal evolution of such a halo can be described via four equations [24]. The derivation follows Jason Pollack [25] and starts from the equations of hydrostatic equilibrium, mass conservation and heat conduction.

3.1.1. Mass Conservation

According to the law of mass conservation, a spherically symmetric mass distribution M at radius r is given by

$$M(r) = \int_0^r 4\pi r'^2 \rho(r')\,\mathrm{d}r', \ r \in [0,\infty) \ , \tag{3}$$

with the corresponding density profile $\rho(r)$. For the purposes of the problem at hand, it is helpful to write this expression in its differential form, which gives the first fundamental

equation

$$\frac{\partial M(r)}{\partial r} = 4\pi r^2 \rho \ . \tag{4}$$

3.1.2. Hydrostatic Equilibrium

It starts from Poisson's equation for gravity

$$\nabla^2 \phi = 4\pi G \rho \ , \tag{5}$$

with the gravitational potential ϕ and the gravitational constant G. Since spherical symmetry is assumed, the Laplace operator can be written as $\nabla^2 \phi = \frac{1}{r^2} \frac{\partial}{\partial r} \left(r^2 \frac{\partial \phi}{\partial r} \right)$, which, together with Equation (4), simplifies to

$$\frac{\partial \phi}{\partial r} = \frac{GM}{r^2} \ . \tag{6}$$

Using the Euler momentum equation for a gravitational potential

$$\frac{\partial \vec{v}}{\partial t} + (\vec{v}\nabla)\vec{v} = -\frac{\nabla p}{\rho} - \nabla \phi \ , \tag{7}$$

and the fact that the flow velocity $\vec{v} = 0$ in a hydrostatic equilibrium, gives the following expression

$$\rho \frac{\partial \phi}{\partial r} = -\frac{\partial p}{\partial r} \ . \tag{8}$$

Assuming a monoatomic ideal gas, its thermal energy per particle is given by the kinetic energy

$$E_{\text{thermal}} = \frac{1}{2} m \langle \vec{v}^2 \rangle = \frac{3}{2} k_B T \ , \tag{9}$$

with the particle mass m, the three-dimensional velocity dispersion $\langle \vec{v}^2 \rangle$, the temperature T and the Boltzmann constant k_B. The corresponding one-dimensional velocity dispersion follows from the relation

$$\nu^2 = \langle v_i^2 \rangle = \frac{1}{3} \langle \vec{v}^2 \rangle = \frac{k_B T}{m} \ , i \in \{x, y, z\} \ . \tag{10}$$

The equation of state for an ideal gas

$$p = \frac{N k_B T}{V} = \frac{\rho}{m} k_B T = \rho \nu^2 \ , \tag{11}$$

together with Equations (6) and (8) gives the second fundamental equation for the hydrostatic equilibrium

$$\frac{\partial \rho \nu^2}{\partial r} = -\frac{GM\rho}{r^2} \ . \tag{12}$$

3.1.3. Heat Transfer

The heat flux ϕ_q, with conduction as transfer method, is given by Fourier's law

$$\phi_q = -\kappa \frac{\partial T}{\partial r} \ , \tag{13}$$

where κ is the thermal conductivity. The corresponding luminosity $L(r)$ is the heat transferred through a sphere of radius r

$$L = 4\pi r^2 \phi_q \ . \tag{14}$$

The combination of these two equations results in the third fundamental equation

$$\frac{L}{4\pi r^2} = -\kappa \frac{\partial T}{\partial r} \ . \tag{15}$$

Since the second law of thermodynamics states, that a transfer in heat results in a change of entropy

$$TdS = dQ \ , \tag{16}$$

an additional equation to describe the system is needed. Starting from Equation (16) and writing it in terms of the specific entropy s

$$T\left(\frac{\partial s}{\partial t}\right)_M = \frac{1}{\rho V}\left(\frac{dQ}{dt}\right)_M = -\frac{1}{\rho}\vec{\nabla}\vec{\phi}_q \ , \tag{17}$$

and using the expression for the luminosity from Equation (14) gives

$$T\left(\frac{\partial s}{\partial t}\right)_M = -\frac{1}{4\pi\rho r^2}\frac{\partial L}{\partial r} \ . \tag{18}$$

Rewriting the first law of thermodynamics to be in terms of the specific entropy s and specific internal energy u yields

$$dU = TdS - pdV \rightarrow du = Tds + \frac{p}{\rho^2}d\rho \ . \tag{19}$$

From this an expression for ds can be obtained

$$ds = \frac{1}{T}\left(du - \frac{p}{\rho^2}d\rho\right) \ . \tag{20}$$

Using Equations (10) and (11) as well as that for an ideal gas $u = \frac{3k_BT}{2m}$, gives

$$ds = \frac{k_B}{m}\left[\frac{3}{2}\frac{dT}{T} - \frac{d\rho}{\rho}\right] \ . \tag{21}$$

Integrating this gives an explicit expression for the specific entropy

$$s = \frac{k_B}{m} \ln\left(\frac{T^{3/2}}{\rho}\right) + \text{const.} \ , \tag{22}$$

which combined with Equations (10) and (18), simplifies to the fourth fundamental equation

$$\frac{\partial L}{\partial r} = -4\pi\rho r^2 \nu^2 \left(\frac{\partial}{\partial t}\right)_M \ln\left(\frac{\nu^3}{\rho}\right) \ . \tag{23}$$

3.1.4. SIDM Gravothermal Fluid

The four derived Equations (4, 12, 15, 23) describe any monoatomic, nonviscous self-gravitating fluid. To distinguish SIDM from other gravothermal fluids like globular clusters, the thermal conductivity needs to be expressed using the cross-section σ [25]. The heat flux $\phi_q(r)$ is the combination of particles moving through a surface at r and their respective thermal energies $\frac{3}{2}k_B T_\pm$ with temperatures T_+ right above the surface and T_- just below the surface. These temperatures, assuming equipartition of energy between particles and using Chapman-Enskog theory, are in first order approximation

$$T_\pm = T(r) \pm b\lambda \frac{\partial T}{\partial r} \ , \tag{24}$$

with $b = 23\sqrt{\pi}/32$ and the mean free path (MFP) λ. Combining equations (13) and (15) and writing the net heat flux in terms of the outwards and inwards moving heat flux gives the following equation

$$\frac{L}{4\pi r^2} = \phi_q(r) = \frac{1}{2}\left[\phi_{q,-} + \phi_{q,+}\right] = \frac{1}{2}\left[\frac{n\lambda}{\tau}\frac{3}{2}k_B T_- - \frac{n\lambda}{\tau}\frac{3}{2}k_B T_+\right] \ , \tag{25}$$

where $\pm\frac{n\lambda}{\tau}$ are the particles fluxes going in and out of the surface.
Using Equation (10), this simplifies to

$$\frac{L}{4\pi r^2} = -\frac{3b\rho\lambda^2}{2\tau}\frac{\partial \nu^2}{\partial r} \ . \tag{26}$$

For this fluid, two regimes are considered. In the short mean free path (SMFP) case, where $\lambda \ll H$ with the Jeans length $H = \sqrt{\frac{\nu^2}{4\pi G\rho}}$ and with $\tau = \frac{\lambda}{\nu}$ the luminosity is given by

$$\frac{L}{4\pi r^2} = -\frac{3b\rho\nu\lambda}{2}\frac{\partial \nu^2}{\partial r} \ , \tag{27}$$

In the long mean free path (LMFP) case, where $\lambda \gg H$, the limits $\lambda \to H$ and $\tau \to t_r$ are adopted, with the relaxation time t_r. The luminosity for this case is defined by

$$\frac{L}{4\pi r^2} = -\frac{3b\rho H^2}{2t_r}\frac{\partial \nu^2}{\partial r} \ . \tag{28}$$

To interpolate between the two regimes, the following relation is adopted from Ref. [26]

$$\kappa^{-1} = \kappa_{\mathrm{SMFP}}^{-1} + \kappa_{\mathrm{LMFP}}^{-1} \ . \tag{29}$$

Inserting this into the heat flux equation gives

$$\frac{L}{4\pi r^2} = -\frac{3b\rho\nu}{2}\left[\frac{1}{\lambda} + \frac{b\nu t_r}{CH^2}\right]^{-1}\frac{\partial\nu^2}{\partial r} \ , \tag{30}$$

where C is a calibrating constant that controls the onset of the core collapse by modulating the significance of the LMFP regime [23].
From the mean free path

$$\lambda = \frac{1}{\rho\sigma_m} \ , \tag{31}$$

follows the relaxation time

$$t_r = (a\rho\sigma_m\nu)^{-1} \ , \tag{32}$$

with $a = \sqrt{16/\pi}$, a constant for hard sphere interactions.
This all results in a form of Equation (15) which describes SIDM halos

$$\frac{L}{4\pi r^2} = -\frac{3ab\sigma_m\nu}{2}\left[a\sigma_m^2 + \frac{4\pi Gb}{C\rho\nu^2}\right]^{-1}\frac{\partial\nu^2}{\partial r} \ . \tag{33}$$

3.1.5. Numerical Implementation

The four equations describing the gravothermal fluid model for SIDM are

$$\frac{\partial M(r)}{\partial r} = 4\pi r^2\rho \ , \tag{34}$$

$$\frac{\partial\rho\nu^2}{\partial r} = -\frac{GM\rho}{r^2} \ , \tag{35}$$

$$\frac{L}{4\pi r^2} = -\frac{3ab\sigma_m\nu}{2}\left[a\sigma_m^2 + \frac{4\pi Gb}{C\rho\nu^2}\right]^{-1}\frac{\partial\nu^2}{\partial r} \ , \tag{36}$$

$$\frac{\partial L}{\partial r} = -4\pi\rho r^2\nu^2\left(\frac{\partial}{\partial t}\right)_M \ln\left(\frac{\nu^3}{\rho}\right) \ . \tag{37}$$

This means there are 6 variables, of which four are dependent $\{M,\ \rho,\ \nu,\ L\}$ on the two independent ones $\{r,\ t\}$.
Introducing dimensionless variables via $\tilde{x} = x/x_0$ with scales

$$M_0 = 4\pi r_s^3\rho_s,\ \nu_0 = \sqrt{\frac{GM_0}{r_s}},\ t_0 = (4\pi\rho_s G)^{-1/2},\ L_0 = \frac{GM_0^2}{r_s t_0},\ \sigma_0 = \frac{4\pi r_s^2}{M_0} \ , \tag{38}$$

where the r_s and ρ_s are the scale radius and density of the halo in question, Equations (34)-(37) can be rewritten as

$$\frac{\partial \tilde{M}}{\partial \tilde{r}} = \tilde{r}^2 \tilde{\rho} \ , \tag{39}$$

$$\frac{\partial \left(\tilde{\rho}\tilde{v}^2\right)}{\partial \tilde{r}} = -\frac{\tilde{M}\tilde{\rho}}{\tilde{r}^2} \ , \tag{40}$$

$$\tilde{L} = -\frac{3}{2} b \tilde{r}^2 \tilde{v} \tilde{\sigma}_m \left(a\tilde{\sigma}_m^2 + \frac{b}{C\tilde{\rho}\tilde{v}^2} \right)^{-1} \frac{\partial \tilde{v}^2}{\partial \tilde{r}} \ , \tag{41}$$

$$\frac{\partial \tilde{L}}{\partial \tilde{r}} = -\tilde{r}^2 \tilde{\rho} \tilde{v}^2 \left(\frac{\partial}{\partial \tilde{t}} \right)_{\tilde{M}} \ln \left(\frac{\tilde{v}^3}{\tilde{\rho}} \right) \ . \tag{42}$$

Solving these equations starts by spatially discretizing the halo into N concentric spherical shells of fixed mass, initially spaced logarithmically between $r_{\min}$ and $r_{\max}$. This leads to two different kinds of quantities, where the extensive ones like $\tilde{M}_i$ and $\tilde{V}_i$ denote the value contained within the radius $\tilde{r}_i$ while $\tilde{L}_i$ gives it at $\tilde{r}_i$. The intensive variables like $\tilde{\rho}_i$, $\tilde{v}_i$, $\tilde{u}_i$ and $\tilde{p}_i$ give the value at the midpoint for the shell they belong to. The evolution of this initial configuration is a loop of two steps. In the first, a heat conduction step is taken by introducing a change to the specific energy $\delta\tilde{u} \simeq -\left(\frac{\partial \tilde{L}}{\partial \tilde{M}}\right) \delta\tilde{t}$, which is obtained by rewriting Equation (42) [23].

The constraint for the time step is set as $\delta\tilde{t} = \epsilon_t \min_{0\le i\le N}(t_{r,i}/t_0)$, with the relaxation time $t_{r,i}$ of the i-th shell and $\epsilon_t = 10^{-4}$. This has the effect of pushing the shells out of hydrostatic equilibrium. To correct this, the adjusted values $\tilde{\rho}_i' = \tilde{\rho}_i + d\tilde{\rho}_i$, $\tilde{p}_i' = \tilde{p}_i + d\tilde{p}_i$ and $\tilde{r}_i' = \tilde{r}_i + d\tilde{r}_i$ need to be calculated for all shells so that

$$2\frac{\tilde{p}_{i+1}' - \tilde{p}_i'}{\tilde{r}_{i+1}' - \tilde{r}_{i-1}'} = -\frac{\tilde{M}_i}{\tilde{r}_i'^2} \frac{\tilde{\rho}_{i+1}' + \tilde{\rho}_i'}{2} \ , \tag{43}$$

is true [23], while preserving the adiabatic invariant $A_i \sim \widetilde{p}_i \tilde{V}_i^{5/3}$ for $i = 1, \ldots, N-1$ in the relaxation process. Mass conservation imposes the condition

$$d\tilde{\rho}_i = -\tilde{\rho}_i \frac{d\tilde{V}_i}{\tilde{V}_i} \ . \tag{44}$$

Since $d\tilde{\rho}_i$ and $d\tilde{p}_i$ can be calculated through $d\tilde{r}$ and $\tilde{r}$

$$d\tilde{\rho}_i = -3\tilde{\rho}_i \frac{\tilde{r}_i^2 d\tilde{r}_i - \tilde{r}_{i-1}^2 d\tilde{r}_{i-1}}{\tilde{r}_i^3 - \tilde{r}_{i-1}^3} \ , \tag{45}$$

$$d\tilde{p}_i = -5\tilde{p}_i \frac{\tilde{r}_i^2 d\tilde{r}_i - \tilde{r}_{i-1}^2 d\tilde{r}_{i-1}}{\tilde{r}_i^3 - \tilde{r}_{i-1}^3} \ , \tag{46}$$

this is a search for a fitting set of $d\tilde{r}_i$. Setting $\tilde{r}_0 = 0$, $\tilde{L}_0 = 0$ and $d\tilde{r}_N = 0$, this can be solved by linearizing Equation (43), yielding a system of $N-1$ tridiagonal equations of the form

$$a_i d\tilde{r}_{i-1} + b_i d\tilde{r}_i + c_i d\tilde{r}_{i+1} = d_i \ , \tag{47}$$

with the constants a_i, b_i, c_i and d_i [23]. The hydrostatic adjustment is taken for every heat conduction step until changes to $\tilde{r}_i$ are so small, that $\epsilon_r > \max_{0<i<N} |d\tilde{r}_i/\tilde{r}_i|$ is satisfied [23] for $\epsilon_r = 10^{-14}$.

3.2. Other Methods

For comparing the results of the gravothermal fluid simulations, two other methods will be used. These are a simulation named Kinetic Spherically Symmetric SIDM (KiSS-SIDM) developed by James Gurian and Simon May [27] as well as an N-body simulation by Moritz Fischer [28].

3.2.1. KiSS-SIDM

This method samples the distribution function with a finite number of tracer particles. These tracers are then used to simulate elastic collisions, with the condition that both scattering tracer have to be in the same cell. The cells are part of a discretized grid making up the halo, with the condition that the cells need to be smaller than the mean free path (MFP). If this condition gets violated by changes to the MFP happening during the evolution, the affected cells get split into two. This splitting also occurs when a fraction of the cells Jeans length, chosen to be 1/20, becomes smaller than the cell itself. A lower limit for cell splitting is set by requiring that each cell contains at least 32 tracers for it to be able to split. There is also an upper limit for collisions in each cell for one time step which is set by

$$\Gamma_i = N_i \rho_i \sigma_{m,\max,i} v_{\max,i} \Delta t \ . \tag{48}$$

Whether particles collide, is determined through rejection sampling of Γ_i random particle pairs, where the condition for a pair to collide is given by

$$\frac{\sigma_m(v_{rel}) v_{rel}}{\sigma_{m,\max,i} v_{\max,i}} > q \tag{49}$$

with an estimate of the cross-section per unit mass $\sigma_{m,\max,i}$ and a random number q drawn from a uniform distribution on [0, 1). It simplifies the problem by assuming

spherical symmetry and thus only tracking the radial position and $\vec{v} = (v_r, v_\phi, v_\theta)$. This leaves the time integration, where each time step gets split

$$K(\Delta t/2)S(\Delta t/2)D(\Delta t)S(\Delta t/2)K(\Delta t/2) \ , \tag{50}$$

with the gravitational kick K, the scattering S and the position update D.
In Ref. [27], Gurian et al. explain that this approach has some advantages when compared to the neighbor search in N-body simulations. The possibility to store and update the cell each particle is in, makes the search for neighbors obsolete, because only particles in the same cell can collide. An upper limit for the distance between two scattering particles is set as the length of the MFP. The last advantage comes from the fact that the maximum number of collisions is proportional to the time step. This means that with smaller time steps the number of collisions also shrinks, making it feasible to adopt time steps much smaller than the scattering timescale, which in turn makes it possible to have global time steps, increasing the energy accuracy [29]. This time step is defined as

$$\Delta t = \min(\Delta t_{\text{coll}}, \Delta t_{\text{grav}}) \ , \tag{51}$$

with the collision time step

$$\Delta t_{\text{coll}} = \min_i \left(\frac{\lambda_{\text{MFP},i}}{v_{\text{max},i}} \right) \ , \tag{52}$$

where $\lambda_{\text{MFP},i}$ is the same as in Equation (31) but uses the density and the estimate of the cross-section per unit mass of the i-th cell. The other one is the gravitational time step

$$\Delta t_{\text{grav}} = \epsilon \min_i(t_{\text{free fall},i}) = \epsilon \min_i \left(\frac{1}{\sqrt{G\tilde{\rho}_i}} \right) \ , \tag{53}$$

where $\epsilon = 0.02$ is chosen.

3.2.2. N-body

The N-body simulations for infrequent scattering, done by Moritz Fischer, use his Pen-Gadget3 module to simulate SIDM [28].
The particles used in the numerical setup represent phase-space patches made up of multiple physical particles. Scattering between two particles can occur when the kernel functions of both overlap. This kernel function $W(r, h)$ represents the DM density distribution of a numerical particle in configuration space [28]. The one used in this

code is a scaled version of the one by Monaghan and Lattanzio [30]. The probability of a physical particle with velocity ν, mass m_χ, travel time t and total cross-section σ moving through a constant density ρ to scatter, is given by

$$P_{\text{scatter}} = \frac{\sigma}{m_\chi}\rho\nu t \ . \tag{54}$$

This means that the expected number of physical particle scattering events for a pair of numerical particles with overlapping kernels and densities ρ_i and ρ_j is

$$\langle N\rangle = \int \frac{\rho_i}{m_\chi} P_{\text{scatter}}\, dV \ . \tag{55}$$

Inserting Equation (54) and the mass of the other particle gives the estimated mass per phase-space that scatters

$$\langle M\rangle = \frac{\sigma}{m_\chi}|\Delta\vec{v}_{ij}|\Delta t \int \rho_i\rho_j\, dV \ , \tag{56}$$

where the relative velocity $\Delta\vec{v}_{ij} = \vec{\nu}_i - \vec{\nu}_j$ and the time step Δt are used.
Since the numerical particles used all have the same mass $m_i = m_j$, the probability for a mass m to scatter is

$$P_{ij} = \frac{\langle M\rangle}{m} = \frac{\sigma}{m_\chi} m|\Delta\vec{v}_{ij}|\Delta t\Lambda_{ij} \ , \tag{57}$$

with the kernel overlap

$$\Lambda_{ij} = \int W(|\vec{x} - \vec{x}_i|,\ h_i) W(|\vec{x} - \vec{x}_j|,\ h_j)\, d\vec{x} \ . \tag{58}$$

To ensure that the code has a good resolution in high number density regions and all particles in low number density regions have at least N_{ngb} neighboring particles to interact with, the kernel size is chosen adaptively.
So, particles scatter if, for a chosen time step, a random number drawn from a uniform distribution on [0, 1) is smaller than P_{ij}. The changes to their respective velocities are defined by

$$\vec{\nu}_i' = \vec{\nu}_{cms} + \frac{|\Delta\vec{v}_{ij}|}{2}\vec{e} \ , \tag{59}$$

and for the second particle

$$\vec{\nu}_j' = \vec{\nu}_{cms} - \frac{|\Delta\vec{v}_{ij}|}{2}\vec{e} \ , \tag{60}$$

using the velocity for the center of mass $\vec{\nu}_{cms} = \frac{\vec{\nu}_i + \vec{\nu}_j}{2}$ and a random normalized vector $\vec{e}$. The time step is defined as

$$\frac{1}{\Delta t} \sim |\Delta v|\frac{\sigma_\uparrow}{m_\chi}\frac{\rho}{N_{\text{ngb}}} \ , \tag{61}$$

with the momentum transfer cross-section

$$\sigma_{\uparrow} = 4\pi \int_0^1 (1 - \cos\theta_{cms}) \frac{\mathrm{d}\sigma}{\mathrm{d}\Omega_{cms}} \,\mathrm{d}\cos\theta_{cms}. \tag{62}$$

The adaptive time step, used in this method, is either defined as

$$\Delta t = \min(\Delta t_i, \Delta t_j) \ , \tag{63}$$

for an active-active particle pair, or as

$$\Delta t = \Delta t_{\text{active}} \ , \tag{64}$$

for an active-passive one.

4. Setup

The goal of this work is to compare different SIDM halo simulation types to get an overview of their validity. This is motivated by the fact that the standard N-body simulations are very expensive both in computational power and the run time. Thus incentivizing the search for a cheaper alternative. The two non N-body methods used in this work are a method by James Gurian and Simon May called KiSS-SIDM [27] as well as the Gravothermal fluid Code developed in Refs. [31], [32], which I used to set up the simulations. The N-body simulations, used as reference, were done by Moritz Fischer using his SIDM module for Gadget3. To get an overview on how the methods perform with different halo masses and time spent in the LMFP regime, three different halos were considered. The parameters describing these are shown in Table 1. The

Table 1: Halo parameters used in the three simulations

Name	M_{halo} [$\mathrm{M}_\odot$]	ρ_s [$\mathrm{M}_\odot\,\mathrm{pc}^{-3}$]	r_s [kpc]	σ_m [$\mathrm{cm}^2\,\mathrm{g}^{-1}$]
Halo1_sig80	2.78×10^9	4.42×10^{-2}	1.28	80.00
Halo1_sig30	2.78×10^9	4.42×10^{-2}	1.28	30.00
Halo2_sig80	3.24×10^7	6.83×10^{-2}	2.51×10^{-1}	80.00

initial conditions of all three simulation methods follow a NFW profile but can vary slightly in the density and in the minimum radius r_{min} of the halo, which can be seen for Halo1_sig80 in Figure 5. While the slightly higher density for KiSS-SIDM in the outer regions is due to the small number of bins used for this plot.

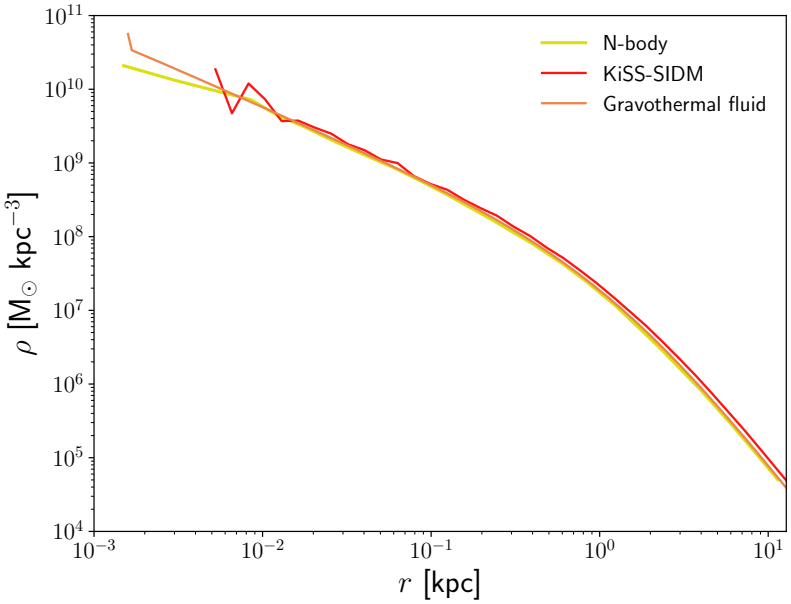

Figure 5: The initial density profile for Halo1_sig80 of all three simulation methods.

4.1. Gravothermal Fluid Initial Parameters

Before starting a simulation with the gravothermal fluid code a few parameters need to be set:

1. r_s [kpc]: scale radius
2. ρ_s [M$_\odot$/pc^3]: scale density
3. C [ ]: calibration constant
4. σ_m [cm^2/g]: interaction cross-section per unit mass
5. n_{shells} [ ]: number of shells to simulate the halo
6. r_{min} [kpc]: minimum radius
7. r_{max} [kpc]: maximum radius
8. t_{end} [ ]: simulation end time

and some more, which will be omitted as they are not relevant to this work. The values used for simulating the three halos can be found in Appendix A.

5. Results

In the following sections the simulation results for the three halos will be presented. The code used for the analysis and plotting can be found at `https://github.com/zjuk/Thesis_analysis_code.git`. The central mass evolution at different radii (left panels) and the relative mass error compared to the N-body simulation (right panels, more information about the error calculations in Appendix B) will be used to compare the methods (Gravothermal fluid, KiSS-SIDM, N-body).

5.1. First Halo

The beginning of the central mass evolution depicted in Figures 6 and 7 shows the LMFP dominated heat transfer in which the halo core forms. This is characterized by the drop in the central mass. The fact that this drop is not present in Figure 8 but rather an almost constant mass, makes it clear that the core never reached a radius of 1.00 kpc. Comparing both KiSS-SIDM and the gravothermal fluid in Figure 7 to the N-body simulation reveals a spike in the relative error (right panel). This spike is caused by an increased rate of mass loss in the center, right at the beginning. While KiSS-SIDM quickly returns to a state where it oscillates around a relative error of zero, the gravothermal fluid needs a bit longer for this.
During the core collapse both methods are similar to the N-body simulation, up until the very end, where the collapse increases greatly in speed and the gravothermal fluid, exhibiting a faster evolution, starts to diverge from both KiSS-SIDM and the N-body.
Since the gravothermal fluid has the calibrating constant C, four different values where chosen to find the best fit, where C controls the onset of the core collapse, so the expectation is that these four runs only start to differ from that point onward. This can be seen in the right panel of Figure 7, where the four graphs start to drift apart from one another.

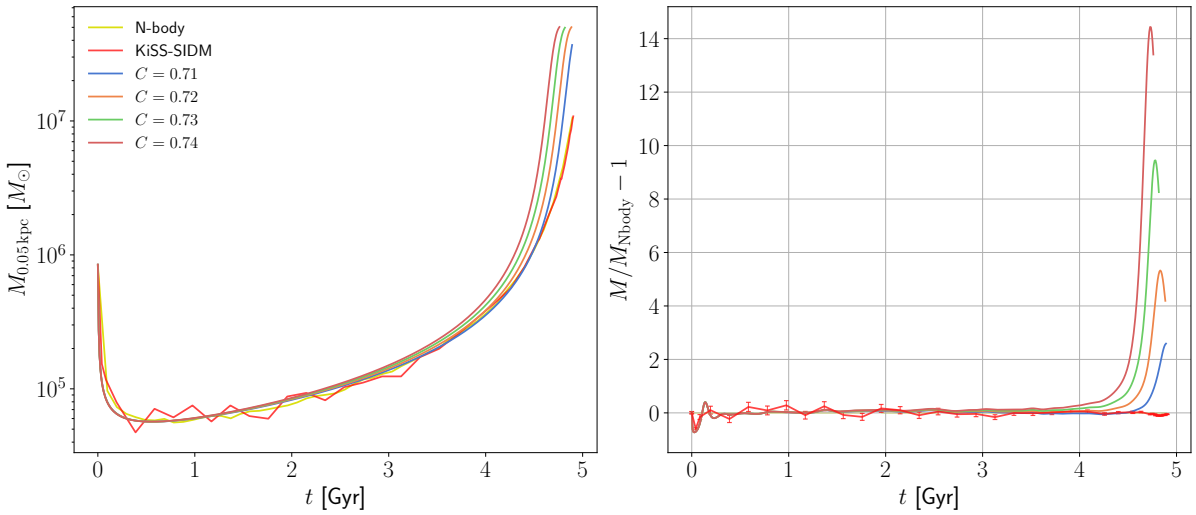

Figure 6: *Left panel*: Central mass evolution of Halo1_sig80 at $r_{\mathrm{enclosed}} = 0.05\,\mathrm{kpc}$ for N-body, KiSS-SIDM and the gravothermal fluid with four different values for C. *Right panel*: The respective relative errors for the enclosed mass compared to the N-body simulation. Also included are the errors for the N-body simulation (green error band) and KiSS-SIDM (red error bars).

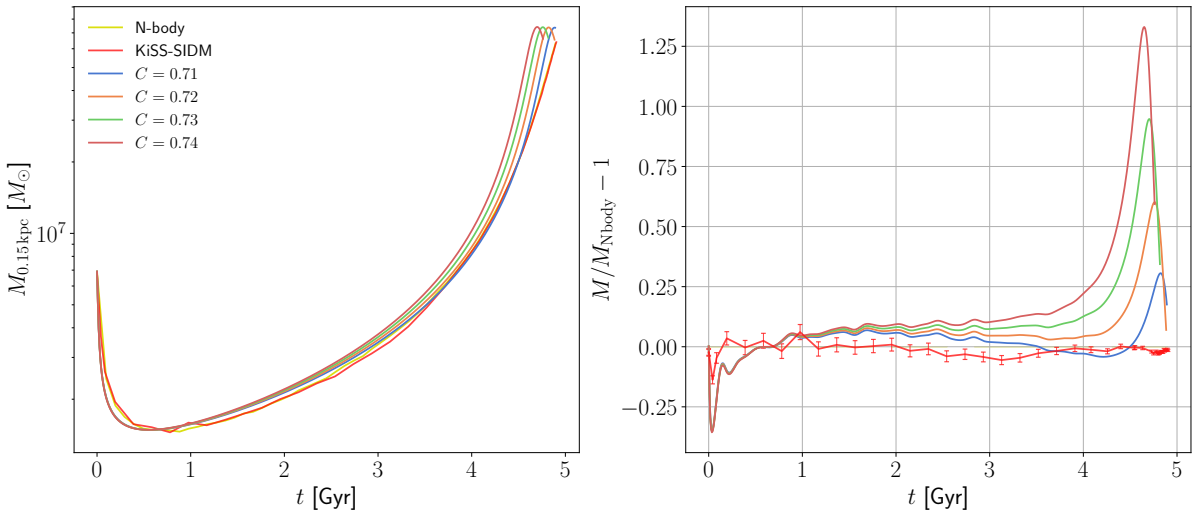

Figure 7: Central mass evolution of Halo1_sig80 at $r_{\mathrm{enclosed}} = 0.15\,\mathrm{kpc}$ for N-body, KiSS-SIDM and the gravothermal fluid with four different values for C.

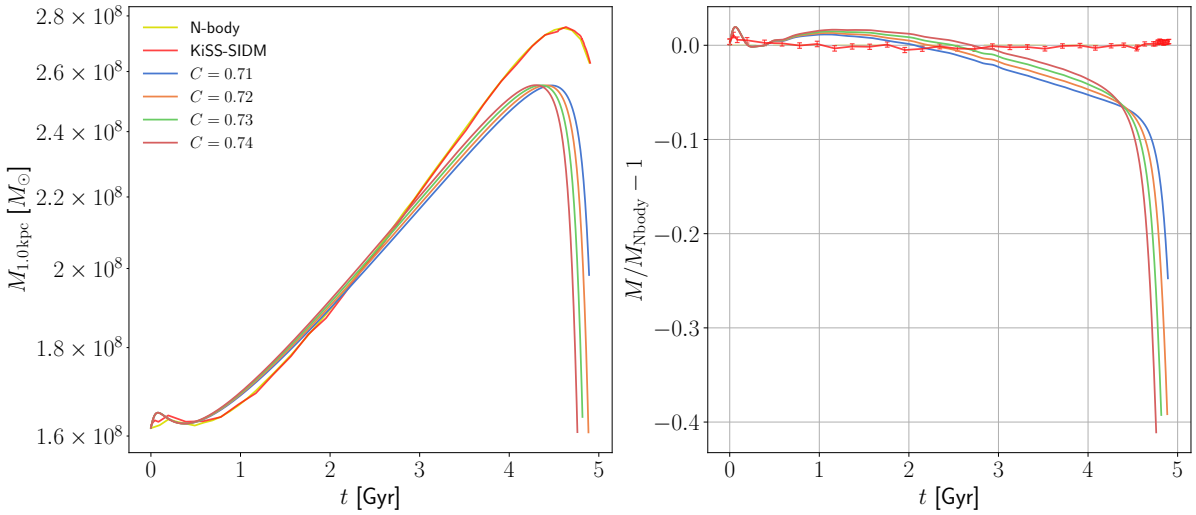

Figure 8: Central mass evolution of Halo1_sig80 at $r_{\mathrm{enclosed}} = 1.00\,\mathrm{kpc}$ for N-body, KiSS-SIDM and the gravothermal fluid with four different values for C.

5.2. Second Halo

The second halo has the same parameters as the one just discussed with σ_m being the only difference between these two. In this case, it is $\sigma_m = 30.00\,\mathrm{cm\,g^{-2}}$, which prolongs the LMFP dominated phase in the early stages of the halo's evolution. Therefore, in this case the time interval examined for this halo is doubled. That is because, through the lower interaction cross-section, the heat transfer is slowed down leading to a generally slower evolution.

The corresponding error for both KiSS-SIDM and the gravothermal fluid for the initial heat transfer phase can be seen in Figures 9 and 10. While the slow core collapse phase is again the phase during the evolution where the relative error for both methods is minimal and around zero, they have problems modelling the faster SMFP core collapse. For the KiSS-SIDM case this faster collapse happens a little bit earlier, but with the huge increases in central mass, this produces a relatively strong discrepancy to the N-body simulation, which is shown in the right panel of Figure 9 and even in Figure 10, though not so significant.

The gravothermal fluid on the other hand exhibits a slower core collapse, this time also for $r_{\mathrm{enclosed}} = 1.00\,\mathrm{kpc}$ in Figure 11, which also leads to larger relative errors. These, however, do not drop as much between Figure 9 and Figure 10 as is the case for the KiSS-SIDM simulation.

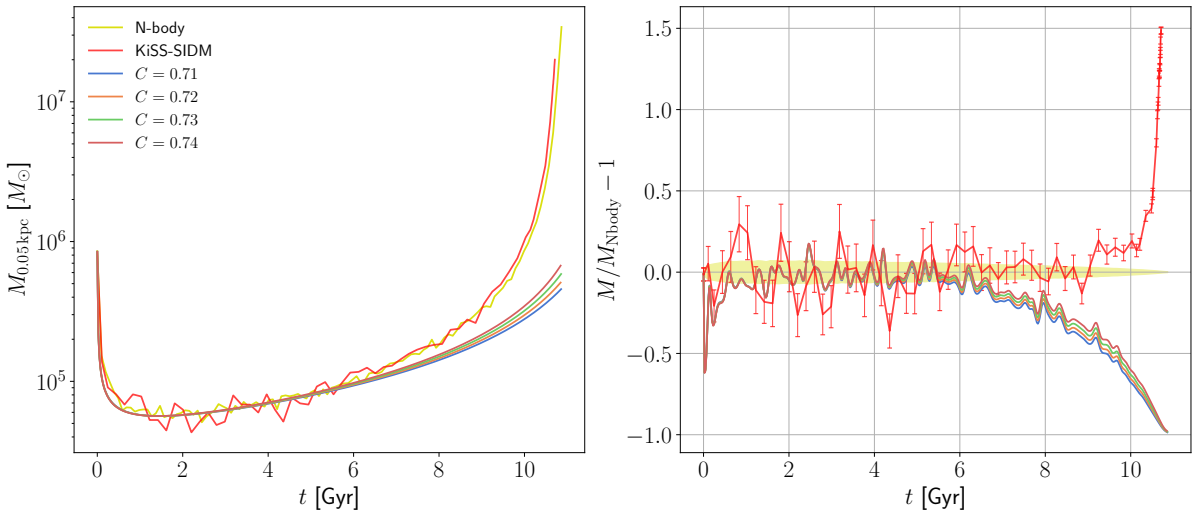

Figure 9: Central mass evolution of Halo1_sig30 at $r_{\mathrm{enclosed}} = 0.05\,\mathrm{kpc}$ for N-body, KiSS-SIDM and the gravothermal fluid with four different values for C.

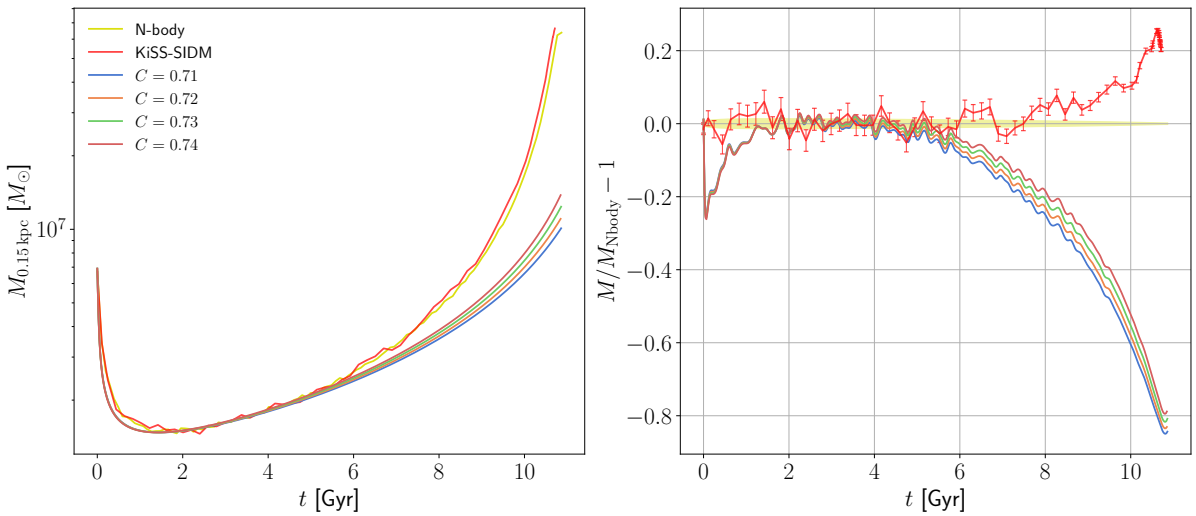

Figure 10: Central mass evolution of Halo1_sig30 at $r_{\mathrm{enclosed}} = 0.15\,\mathrm{kpc}$ for N-body, KiSS-SIDM and the gravothermal fluid with four different values for C.

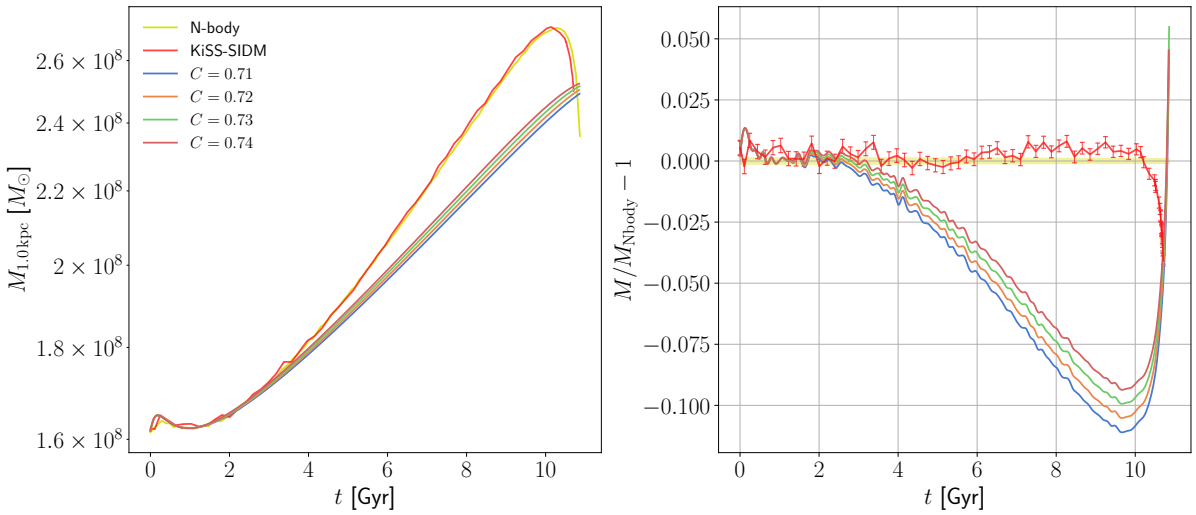

Figure 11: Central mass evolution of Halo1_sig30 at $r_{\mathrm{enclosed}} = 1.00\,\mathrm{kpc}$ for N-body, KiSS-SIDM and the gravothermal fluid with four different values for C.

5.3. Third Halo

The third halo has a similar evolution timescale as the second one. While the gravothermal fluid still has problems at modelling the early core formation, which can be seen in Figure 12 and a slower core collapse resulting in an increasing discrepancy to the N-body data, which can also be seen in Figure 13, KiSS-SIDM now generally overestimates the central mass compared to the N-body simulation, while also exhibiting a slightly faster collapse. For the case of $r_{\mathrm{enclosed}} = 1.00\,\mathrm{kpc}$, shown in Figure 14, the changes in the mass are relatively small, resulting in overall low errors, but with KiSS-SIDM being better at modeling the trend of the N-body simulation.

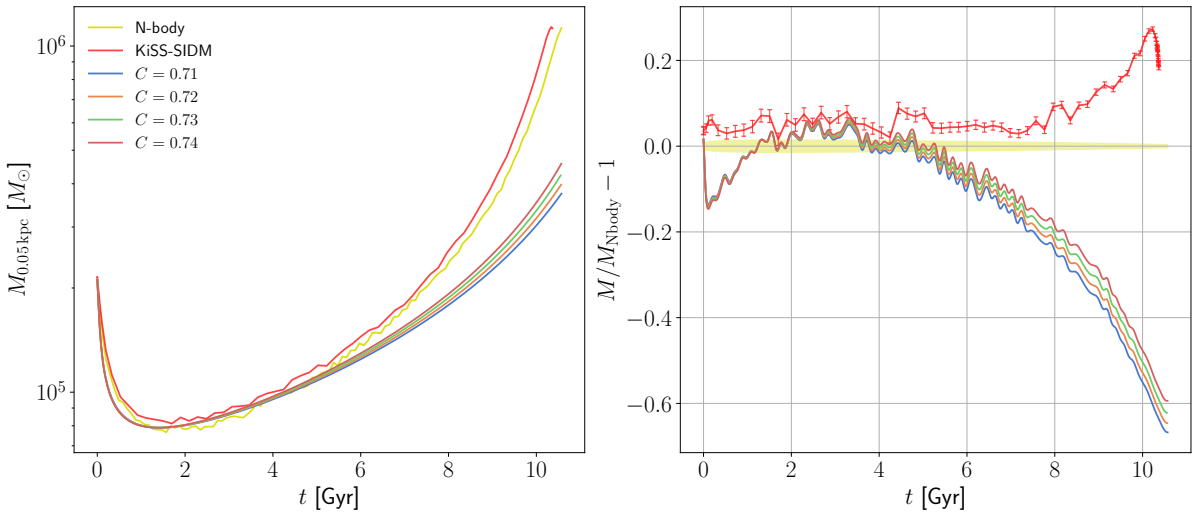

Figure 12: Central mass evolution of Halo2_sig80 at $r_{\mathrm{enclosed}} = 0.05\,\mathrm{kpc}$ for N-body, KiSS-SIDM and the gravothermal fluid with four different values for C.

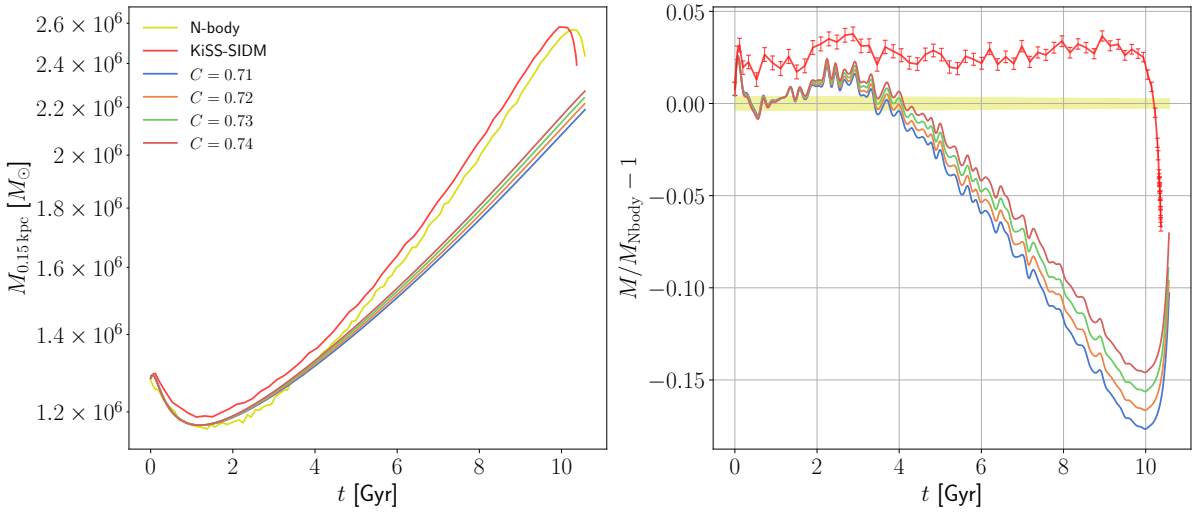

Figure 13: Central mass evolution of Halo2_sig80 at $r_{\mathrm{enclosed}} = 0.15\,\mathrm{kpc}$ for N-body, KiSS-SIDM and the gravothermal fluid with four different values for C.

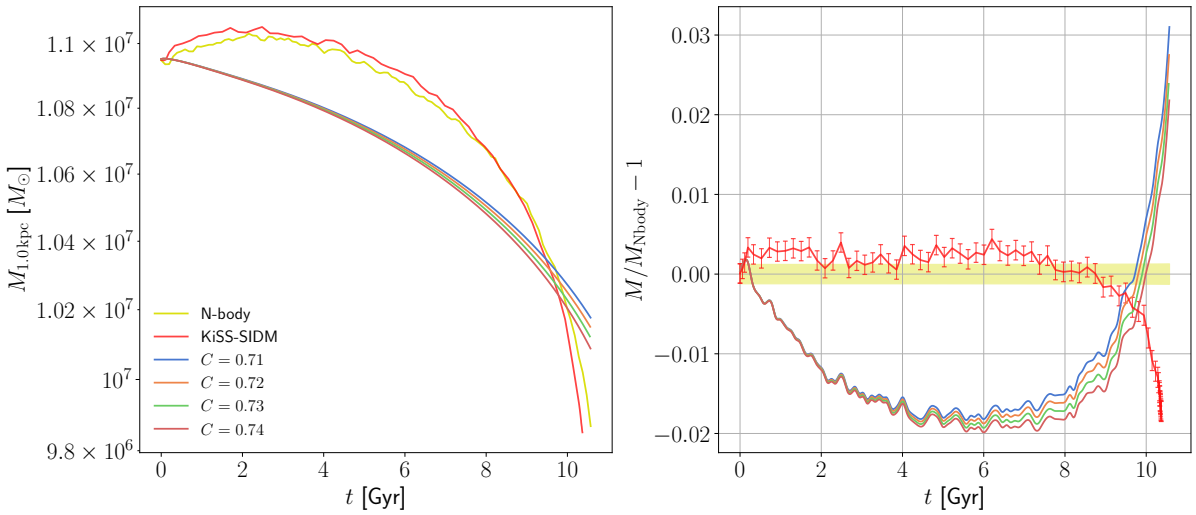

Figure 14: Central mass evolution of Halo2_sig80 at $r_{\mathrm{enclosed}} = 1.00\,\mathrm{kpc}$ for N-body, KiSS-SIDM and the gravothermal fluid with four different values for C.

5.4. Changing the Thermal Conductivity

In their paper Nishikawa et al. [23] stated that the key problem of the gravothermal fluid method most likely stems from the interpolation of κ between the two mean free path regimes. Thus, they proposed to use the more general form instead

$$\kappa^{-\alpha} = \kappa_{\mathrm{LMFP}}^{-\alpha} + \kappa_{\mathrm{SMFP}}^{-\alpha} \ . \tag{65}$$

For $\alpha = 1$ the original interpolation scheme gets recovered, but $\alpha \neq 1$ results in changes to the evolution, which, paired with an adjusted value for C, can result in faster evolutions with a decreased influence of the SMFP regime [23] and potentially increasing the accuracy of this method.

Using Equation (65) for the interpolation of the thermal conductivity, Equation (41) changes to

$$\tilde{L} = -\frac{3}{2} ab \frac{\tilde{r}^2 \tilde{\rho} \tilde{v}^3}{\tilde{\sigma}_m} \left(1 + \left(\frac{aC}{b} \tilde{\sigma_m}^2 \tilde{\rho} \tilde{v}^2 \right)^{\alpha} \right)^{-1/\alpha} \frac{\partial \tilde{v}^2}{\partial \tilde{r}} \ . \tag{66}$$

Simulating a few halos for Halo1_sig80 with different combinations of α and C enables an interpolation of these runs for a different parameter combination. Minimizing the mean squared difference between the mass contained in a sphere of radius $r_{0.05\mathrm{kpc}}$ for the interpolated run and the N-body simulation, is used to find a new parameter pair, which came out as $\alpha = 0.512$ and $C = 0.885$ using as initial data the simulations with the parameters listed in Table 2.

Table 2: Initial parameter pairs

α	0.4	0.4	0.6	0.8
C	0.95	1.2	0.8	0.753

The following figures show the different combinations of α and C for the first Halo. The two runs, using $\alpha = 0.512, C = 0.885$ and $\alpha = 0.6, C = 0.8$ are able to model the evolution really well for the smaller radii but show problems at modeling the early mass transfer, seen in the two big spikes for the differences compared to the N-body simulation in the right panel of Figure 15. While the KiSS-SIDM simulation just has the first spike it does not have the second one.

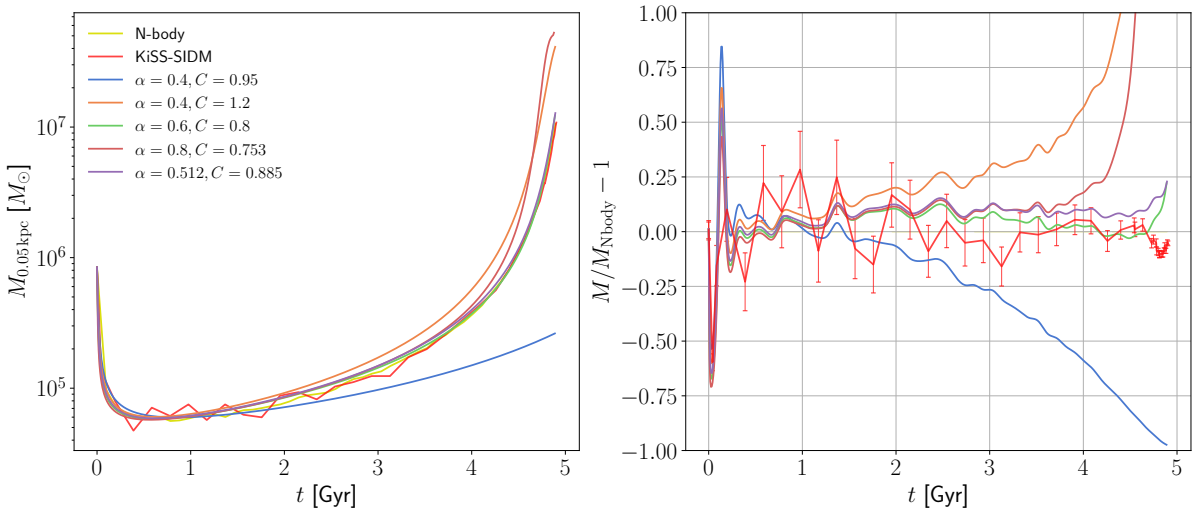

Figure 15: Central mass evolution of Halo1_sig80 at $r_{\mathrm{enclosed}} = 0.05\,\mathrm{kpc}$ for N-body, KiSS-SIDM and the gravothermal fluid with five different value pairs for α and C.

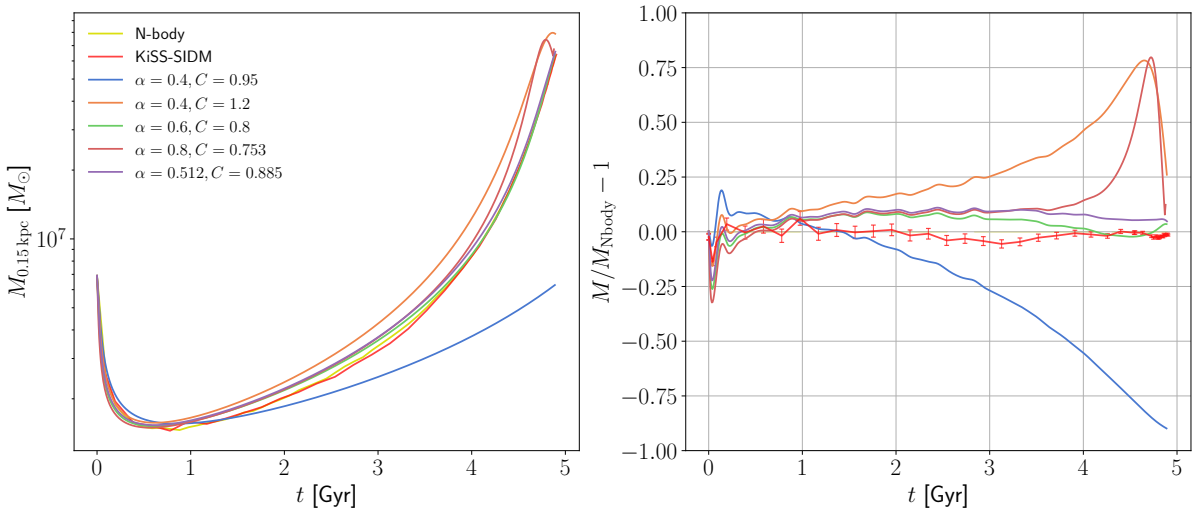

Figure 16: Central mass evolution of Halo1_sig80 at $r_{\mathrm{enclosed}} = 0.15\,\mathrm{kpc}$ for N-body, KiSS-SIDM and the gravothermal fluid with five different value pairs for α and C.

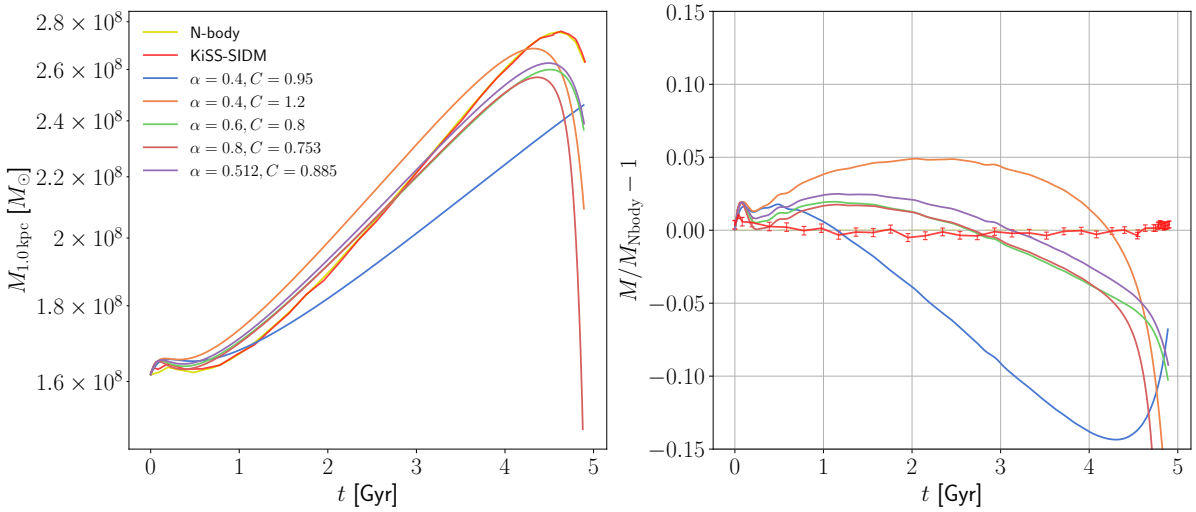

Figure 17: Central mass evolution of Halo1_sig80 at $r_{\mathrm{enclosed}} = 1.00\,\mathrm{kpc}$ for N-body, KiSS-SIDM and the gravothermal fluid with five different value pairs for α and C.

To see how well these parameters are at modelling the other two halos, choosing for example $r_{\mathrm{enclosed}} = 0.05\,\mathrm{kpc}$ of Halo2_sig80, seen in Figure 21, it shows that $\alpha = 0.512, C = 0.885$ is able to match and even outperform KiSS-SIDM in this case. But both models have trouble simulating Halo1_sig30 for the two smaller radii (Figure 18 and 19).

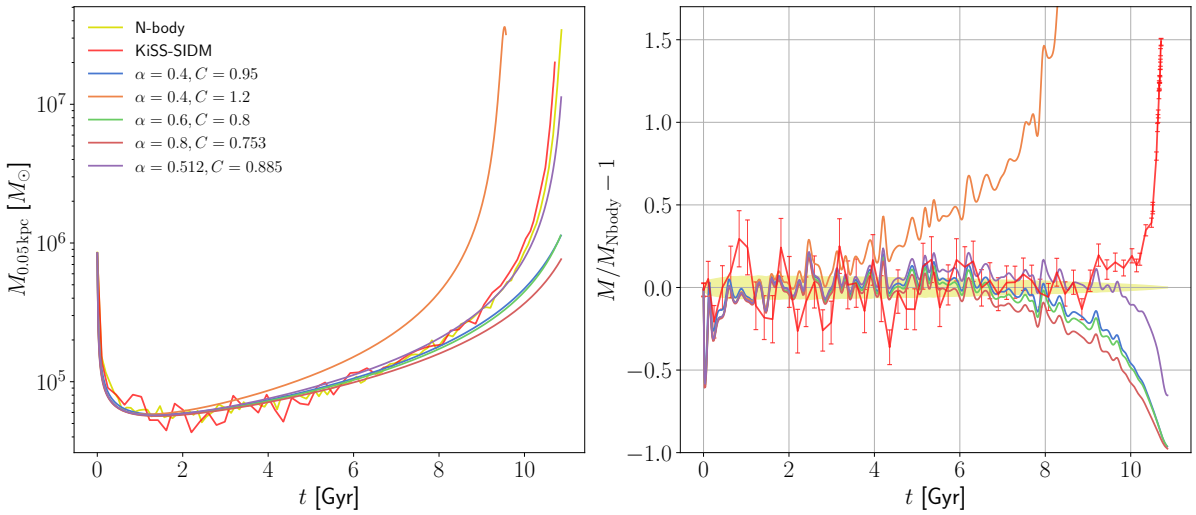

Figure 18: Central mass evolution of Halo1_sig30 at $r_{\mathrm{enclosed}} = 0.05\,\mathrm{kpc}$ for N-body, KiSS-SIDM and the gravothermal fluid with five different value pairs for α and C.

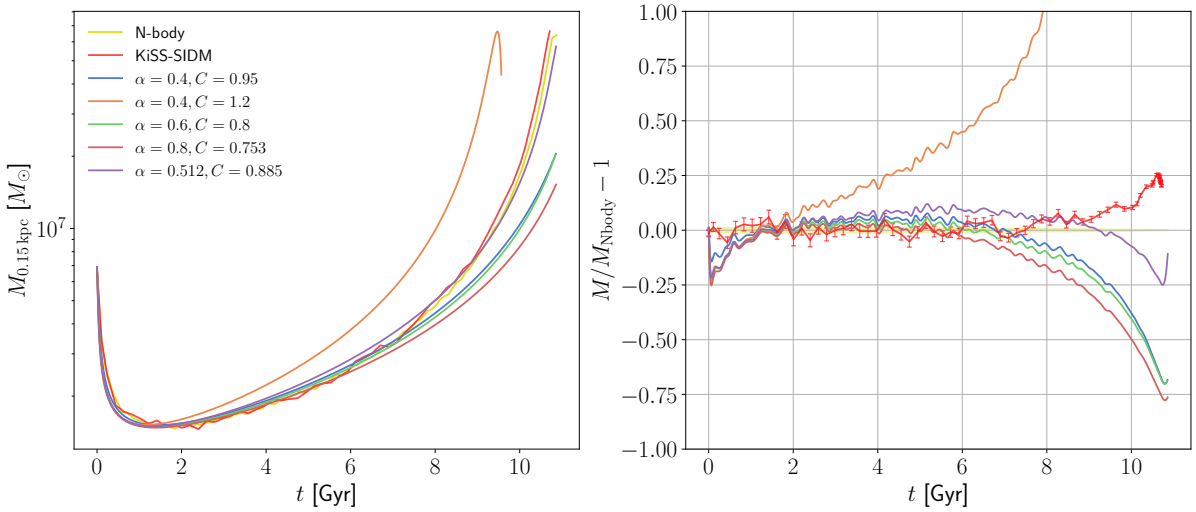

Figure 19: Central mass evolution of Halo1_sig30 at $r_{\mathrm{enclosed}} = 0.15\,\mathrm{kpc}$ for N-body, KiSS-SIDM and the gravothermal fluid with five different value pairs for α and C.

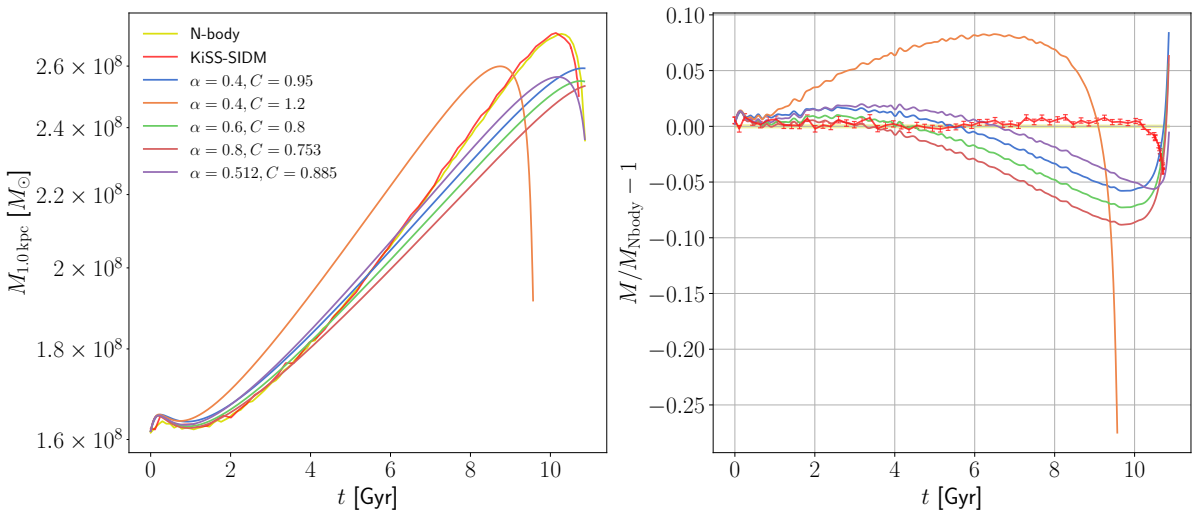

Figure 20: Central mass evolution of Halo1_sig30 at $r_{\mathrm{enclosed}} = 1.00\,\mathrm{kpc}$ for N-body, KiSS-SIDM and the gravothermal fluid with five different value pairs for α and C.

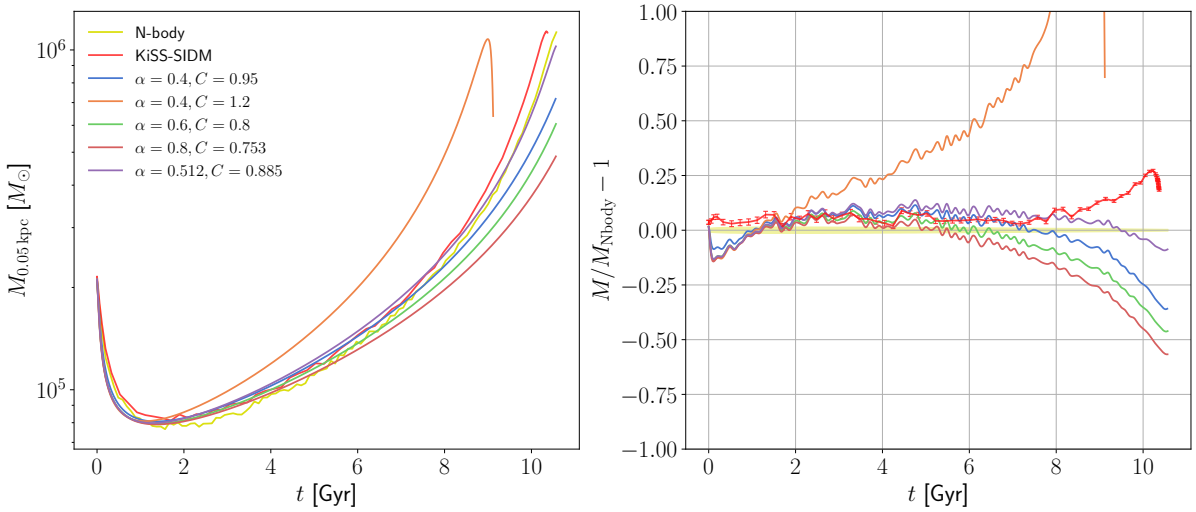

Figure 21: Central mass evolution of Halo2_sig80 at $r_{\mathrm{enclosed}} = 0.05\,\mathrm{kpc}$ for N-body, KiSS-SIDM and the gravothermal fluid with five different value pairs for α and C.

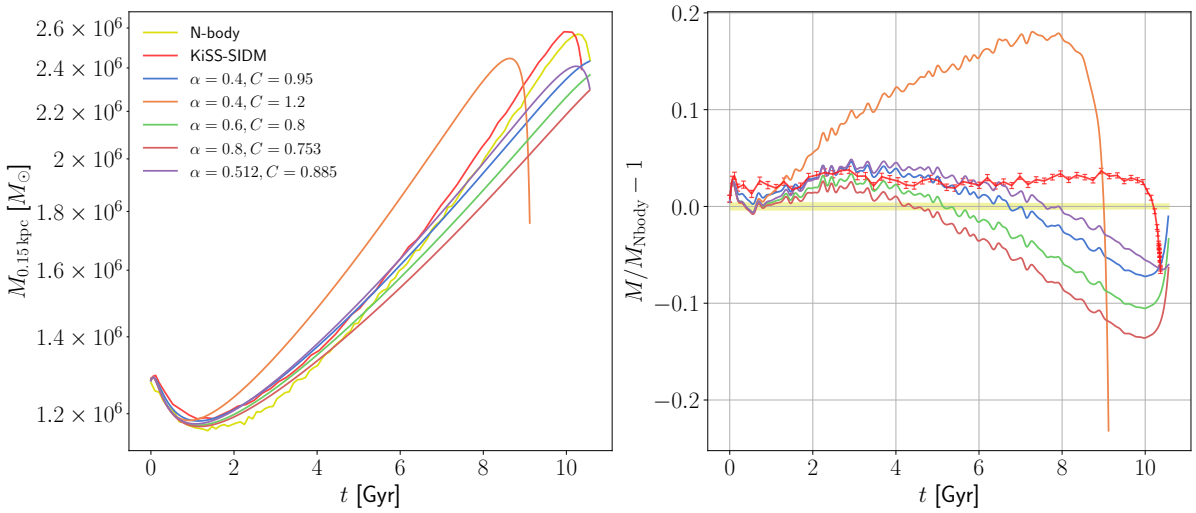

Figure 22: Central mass evolution of Halo2_sig80 at $r_{\mathrm{enclosed}} = 0.15\,\mathrm{kpc}$ for N-body, KiSS-SIDM and the gravothermal fluid with five different value pairs for α and C.

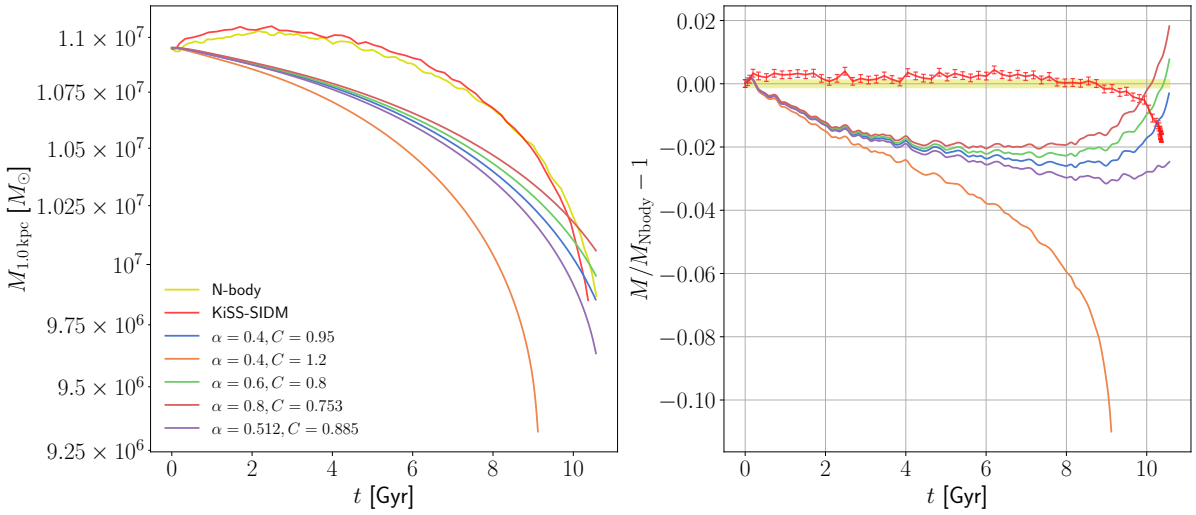

Figure 23: Central mass evolution of Halo2_sig80 at $r_{\mathrm{enclosed}} = 1.00\,\mathrm{kpc}$ for N-body, KiSS-SIDM and the gravothermal fluid with five different value pairs for α and C.

6. Conclusions

This work serves to find a general calibration of the gravothermal fluid method for simulating the core collapse of SIDM halos by comparing it to an N-body simulation and another method called KiSS-SIDM. The free parameters available for this are the calibration constant C and the scaling of the heat conductivity interpolation between the

SMFP and LMFP regime.
The quality of the gravothermal fluid simulations for the three halos using just the calibration constant C as a free initial parameter does not reach an acceptable level of accuracy. This is caused by the problems this method displays at simulating the early mass transfer phase as well as the difficulties predominantly with the SMFP core collapse. While the first problem is the same for all three halos considered, where a faster mass transfer for the gravothermal fluid leads to a spike in the relative error, this is not the case for the core collapse. While for Halo1_sig80 the four gravothermal fluid runs exhibit a faster collapse, for the other two halos it is the exact opposite, where now the halo collapses slower than in the N-body simulation.
Although changing the interpolation used for the heat conductivity κ to a more general form using α, produces good results for the first (Halo1_sig80) and third halo (Halo2_sig80) using $\alpha = 0.512$ and $C = 0.885$, it can not simulate the steep central mass increase during the late phases of the core collapse of the second halo as well. This shows the difficulty of the gravothermal fluid method at finding a general calibration which produces good fits for a wide array of halos. Making it clear that for the gravothermal fluid approach to be a viable option for faster SIDM halo simulation, further development of the method regarding the calibration and interpolation of the heat conductivity to also accurately model halos like Halo1_sig30 is required.
Also, KiSS-SIDM seems to be a promising alternative, which, for the most part, produces results very close to the N-body simulations, although it also seemed to struggle with the very steep central mass increase during the late phases of the core collapse of the second halo.

A. List of Parameters used for the Gravothermal Fluid Code Runs

Table 3: Initial parameters used for the gravothermal fluid simulations

Parameter	Halo1_sig30	Halo1_sig80	Halo2_sig80
r_s [kpc]	1.28	1.28	0.25
ρ_s [$M_\odot/pc^3$]	4.42×10^{-2}	4.42×10^{-2}	6.83×10^{-2}
σ_m [cm^2/g]	80.00	30.00	80.00
n_{shells} [ ]	200.00	200.00	200.00
$r_{\min}$ [kpc]	1.28×10^{-3}	1.28×10^{-3}	2.51×10^{-3}
$r_{\max}$ [kpc]	19.20	19.20	19.20
$\tilde{t}_{\text{end}}$ [ ]	255.00	555.00	690.00

B. Error for Gravothermal Fluid Code

One of the interesting graphs for the halo simulation is the evolution of the central mass contained in a sphere of radius r_{enclosed}. This is done in the N-body simulation by adding the masses of all shells contained in the sphere with radius $r = r_{\text{enclosed}}$ and in KiSS-SIDM by adding up the mass of all particles contained in this sphere. The error for this method is the mass divided by the square-root of the number of particles contained. Since the N-body simulation does this using shells, the different errors are combined using this equation

$$\Delta m = \sqrt{\sum_{i=1}^{N} \Delta m_i^2} \ . \tag{67}$$

While in the gravothermal fluid approach the halo also gets discretized into separate spheres, where the code gives out their respective masses. The central mass as a function of the radius is made up of discrete points and not continuous, thus, in general, an error is introduced because of differences in the chosen outer radius $r_{\text{enclosed, gravothermal}} \neq r_{\text{enclosed}}$. For the plots in the results section, a cubic spline was used to interpolate the mass of the gravothermal fluid halo at r_{enclosed}.

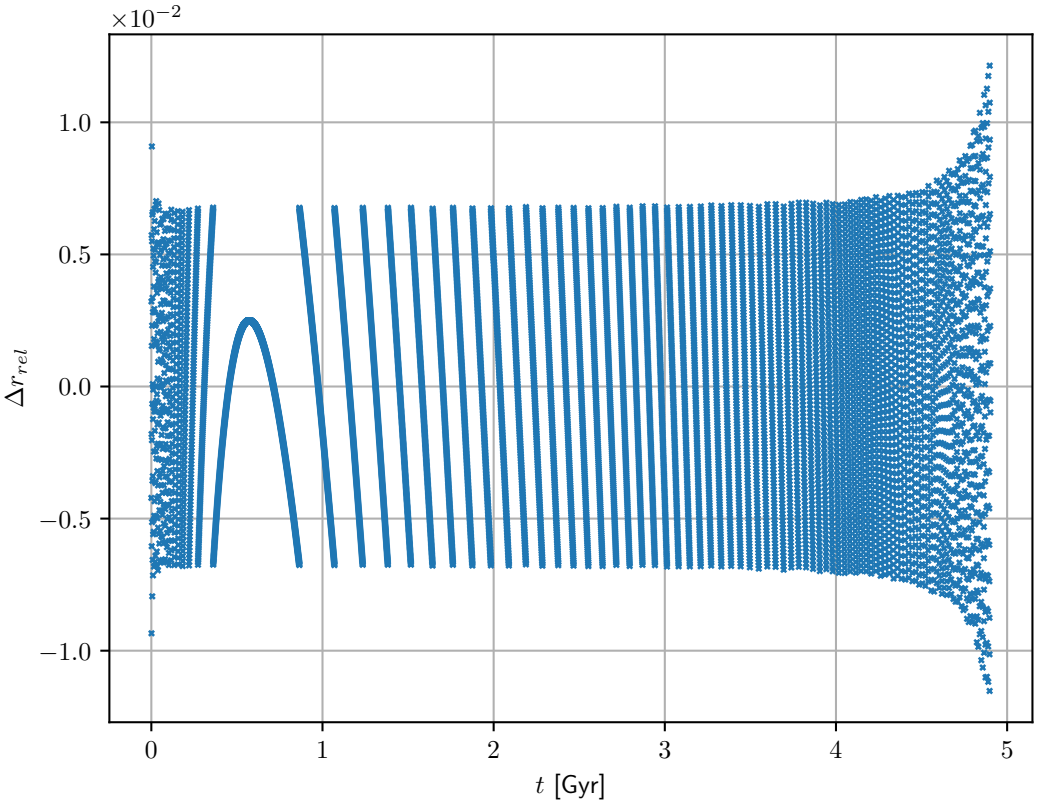

Figure 24: The relative error for the chosen outer radius of the gravothermal fluid compared to r_{enclosed} using $n_{\text{shells}} = 450$ for Halo1_sig80.

This graph shows, by looking at the structure of the error, how the gravothermal fluid code works. It starts relatively random until the error starts to move along vertical lines with an increasing tilt to the right side. Starting a new line, means that a new shell is now the closest to the chosen radius. With advancing time, mass streams from the center outwards, and with it the shells, resulting in the error first getting smaller as the shell gets closer to the chosen radius. With the shell now moving past r_{enclosed}, the error starts growing. When the shell moves too far, a new shell is now the best fit and the whole thing repeats until the minimum of the central mass is reached and the mass in the halo begins to flow back into the center, starting the gravothermal collapse. This turning point, where the shells now start to move towards the center, is represented by the arch around 0.50 Gyr. Now the almost vertical lines start again, but this time tilted to the left and losing tilt over time, as the collapse speeds up. At 4.00 Gyr, the maximum error increases as the nearest shells are now getting bigger.

Looking at the index of the chosen outer radius and plotting it over the whole evolution, as shown in Figure 25, results in a graph which is very similar to the central mass evolution of the halo (see Figure 7).

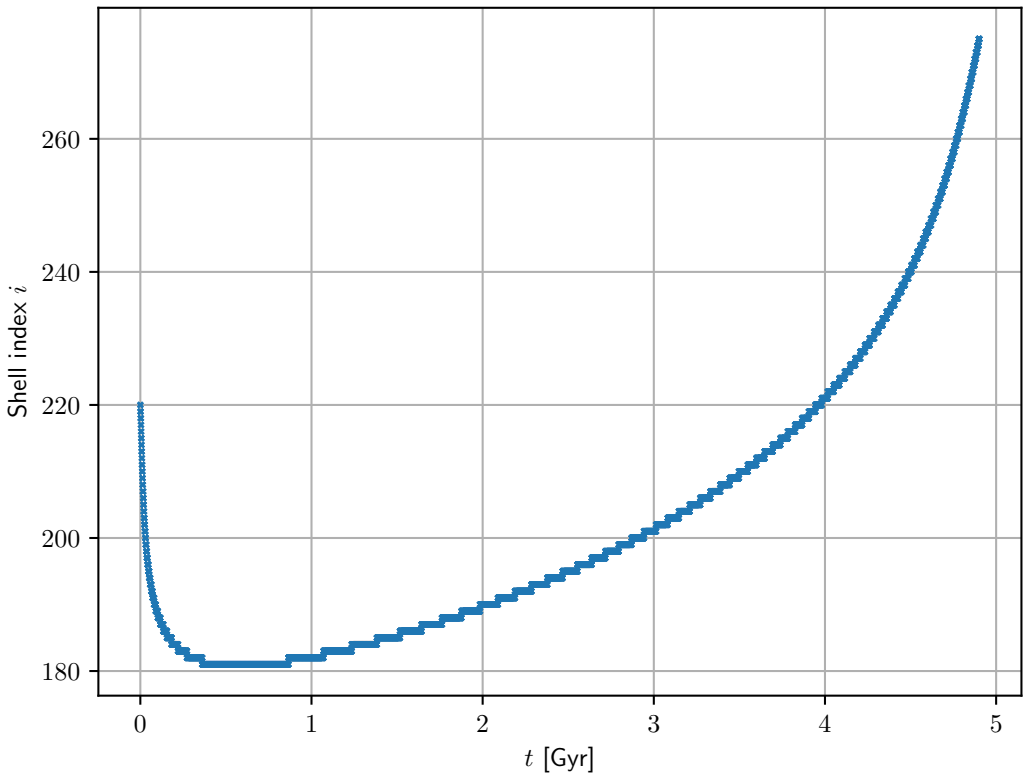

Figure 25: Index of the shell closest to r_{enclosed} plotted over the duration of the evolution using $n_{\text{shells}} = 450$ for Halo1_sig80.

References

[1] L. Sagunski, "Kosmologie", Lecture notes, Goethe Universität Frankfurt am Main, accessed 25.07.2025.

[2] M. S. Turner, *ΛCDM: Much more than we expected, but now less than what we want*, arXiv:2109.01760, Sep. 2021. DOI: 10.48550/arXiv.2109.01760. Accessed: Aug. 21, 2025. [Online]. Available: http://arxiv.org/abs/2109.01760.

[3] W. J. G. de Blok, "The core-cusp problem", *Advances in Astronomy*, vol. 2010, no. 1, E. Brinks, Ed., Nov. 2009, ISSN: 1687-7977. DOI: 10.1155/2010/789293. [Online]. Available: http://dx.doi.org/10.1155/2010/789293.

[4] A. Klypin, A. V. Kravtsov, O. Valenzuela, and F. Prada, "Where are the missing galactic satellites?", *The Astrophysical Journal*, vol. 522, no. 1, pp. 82–92, Sep. 1999, ISSN: 1538-4357. DOI: 10.1086/307643. [Online]. Available: http://dx.doi.org/10.1086/307643.

[5] D. N. Spergel and P. J. Steinhardt, "Observational evidence for self-interacting cold dark matter", *Physical Review Letters*, vol. 84, no. 17, pp. 3760–3763, Apr. 2000, ISSN: 1079-7114. DOI: 10.1103/physrevlett.84.3760. [Online]. Available: http://dx.doi.org/10.1103/PhysRevLett.84.3760.

[6] J. Pollack, D. N. Spergel, and P. J. Steinhardt, "Supermassive black holes from ultra-strongly self-interacting dark matter", *The Astrophysical Journal*, vol. 804, no. 2, p. 131, May 2015, ISSN: 1538-4357. DOI: 10.1088/0004-637x/804/2/131. [Online]. Available: http://dx.doi.org/10.1088/0004-637X/804/2/131.

[7] P. Collaboration, *Planck 2018 results. vi. cosmological parameters*, 2021. DOI: https://doi.org/10.1051/0004-6361/201833910. arXiv: 1807.06209 [astro-ph.CO]. [Online]. Available: https://arxiv.org/abs/1807.06209.

[8] J. A. Vazquez, L. E. Padilla, and T. Matos, *Inflationary cosmology: From theory to observations*, 2021. DOI: https://doi.org/10.31349/RevMexFisE.17.73. arXiv: 1810.09934 [astro-ph.CO]. [Online]. Available: https://arxiv.org/abs/1810.09934.

[9] L. M. Krauss and B. Chaboyer, *New globular cluster age estimates and constraints on the cosmic equation of state and the matter density of the universe*, 2001. arXiv: astro-ph/0111597 [astro-ph]. [Online]. Available: https://arxiv.org/abs/astro-ph/0111597.

[10] A. G. Riess et al., "Observational evidence from supernovae for an accelerating universe and a cosmological constant", *The Astronomical Journal*, vol. 116, no. 3, pp. 1009–1038, Sep. 1998, ISSN: 0004-6256. DOI: 10.1086/300499. [Online]. Available: http://dx.doi.org/10.1086/300499.

[11] F. Zwicky, "Die Rotverschiebung von extragalaktischen Nebeln", *Helvetica Physica Acta*, vol. 6, pp. 110–127, Jan. 1933.

[12] P. J. E. Peebles, "Large-scale background temperature and mass fluctuations due to scale-invariant primeval perturbations", vol. 263, pp. L1–L5, Dec. 1982. DOI: 10.1086/183911.

[13] G. R. Blumenthal, S. M. Faber, J. R. Primack, and M. J. Rees, "Formation of galaxies and large-scale structure with cold dark matter.", vol. 311, pp. 517–525, Oct. 1984. DOI: 10.1038/311517a0.

[14] G. Kauffmann, S. D. M. White, and B. Guiderdoni, "The formation and evolution of galaxies within merging dark matter haloes.", vol. 264, pp. 201–218, Sep. 1993. DOI: 10.1093/mnras/264.1.201.

[15] B. Moore et al., "Dark matter substructure within galactic halos", *The Astrophysical Journal*, vol. 524, no. 1, pp. L19–L22, Oct. 1999, ISSN: 0004-637X. DOI: 10.1086/312287. [Online]. Available: http://dx.doi.org/10.1086/312287.

[16] K. Bechtol et al., "Eight new milky way companions discovered in first-year dark energy survey data", *The Astrophysical Journal*, vol. 807, no. 1, p. 50, Jun. 2015, ISSN: 1538-4357. DOI: 10.1088/0004-637x/807/1/50. [Online]. Available: http://dx.doi.org/10.1088/0004-637X/807/1/50.

[17] S. Jeon et al., *Born to be starless: Revisiting the missing satellite problem*, 2025. arXiv: 2506.09152 [astro-ph.GA]. [Online]. Available: https://arxiv.org/abs/2506.09152.

[18] A. M. Brooks, M. Kuhlen, A. Zolotov, and D. Hooper, "A baryonic solution to the missing satellites problem", *The Astrophysical Journal*, vol. 765, no. 1, p. 22, Feb. 2013, ISSN: 1538-4357. DOI: 10.1088/0004-637x/765/1/22. [Online]. Available: http://dx.doi.org/10.1088/0004-637X/765/1/22.

[19] J. F. Navarro, C. S. Frenk, and S. D. M. White, "The structure of cold dark matter halos", *The Astrophysical Journal*, vol. 462, p. 563, May 1996, ISSN: 1538-4357. DOI: 10.1086/177173. [Online]. Available: http://dx.doi.org/10.1086/177173.

[20] S. Tulin and H.-B. Yu, "Dark matter self-interactions and small scale structure", *Physics Reports*, vol. 730, pp. 1–57, Feb. 2018, ISSN: 0370-1573. DOI: 10.1016/j.physrep.2017.11.004. [Online]. Available: http://dx.doi.org/10.1016/j.physrep.2017.11.004.

[21] A. H. G. Peter, M. Rocha, J. S. Bullock, and M. Kaplinghat, "Cosmological simulations with self-interacting dark matter – ii. halo shapes versus observations", *Monthly Notices of the Royal Astronomical Society*, vol. 430, no. 1, pp. 105–120, Jan. 2013, ISSN: 0035-8711. DOI: 10.1093/mnras/sts535. [Online]. Available: http://dx.doi.org/10.1093/mnras/sts535.

[22] J. Zavala, M. Vogelsberger, and M. G. Walker, "Constraining self-interacting dark matter with the milky way's dwarf spheroidals", *Monthly Notices of the Royal Astronomical Society: Letters*, vol. 431, no. 1, pp. L20–L24, Feb. 2013, ISSN: 1745-3925. DOI: 10.1093/mnrasl/sls053. [Online]. Available: http://dx.doi.org/10.1093/mnrasl/sls053.

[23] H. Nishikawa, K. K. Boddy, and M. Kaplinghat, "Accelerated core collapse in tidally stripped self-interacting dark matter halos", *Physical Review D*, vol. 101, no. 6, Mar. 2020, ISSN: 2470-0029. DOI: 10.1103/physrevd.101.063009. [Online]. Available: http://dx.doi.org/10.1103/PhysRevD.101.063009.

[24] D. Lynden-Bell and P. P. Eggleton, "On the consequences of the gravothermal catastrophe", vol. 191, pp. 483–498, May 1980. DOI: 10.1093/mnras/191.3.483.

[25] J. Pollack, *Supermassive black holes from gravothermal collapse of fractional self-interacting dark matter halos*, 2012.

[26] S. Balberg, S. L. Shapiro, and S. Inagaki, "Self-interacting dark matter halos and the gravothermal catastrophe", *The Astrophysical Journal*, vol. 568, no. 2, pp. 475–487, Apr. 2002, ISSN: 1538-4357. DOI: 10.1086/339038. [Online]. Available: http://dx.doi.org/10.1086/339038.

[27] J. Gurian and S. May, *Core collapse beyond the fluid approximation: The late evolution of self-interacting dark matter halos*, 2025. arXiv: 2505.15903 [astro-ph.CO]. [Online]. Available: https://arxiv.org/abs/2505.15903.

[28] M. S. Fischer et al., "N-body simulations of dark matter with frequent self-interactions", vol. 505, no. 1, pp. 851–868, Jul. 2021. DOI: 10.1093/mnras/stab1198. arXiv: 2012.10277 [astro-ph.CO].

[29] M. S. Fischer, K. Dolag, and H.-B. Yu, "Numerical challenges for energy conservation in n-body simulations of collapsing self-interacting dark matter halos", *Astronomy & Astrophysics*, vol. 689, A300, Sep. 2024, ISSN: 1432-0746. DOI: 10.1051/0004-6361/202449849. [Online]. Available: http://dx.doi.org/10.1051/0004-6361/202449849.

[30] J. J. Monaghan and J. C. Lattanzio, "A refined particle method for astrophysical problems", vol. 149, no. 1, pp. 135–143, Aug. 1985.

[31] N. J. Outmezguine, K. K. Boddy, S. Gad-Nasr, M. Kaplinghat, and L. Sagunski, "Universal gravothermal evolution of isolated self-interacting dark matter halos for velocity-dependent cross-sections", *Monthly Notices of the Royal Astronomical Society*, vol. 523, no. 3, pp. 4786–4800, Jun. 2023, ISSN: 1365-2966. DOI: 10.1093/mnras/stad1705. [Online]. Available: http://dx.doi.org/10.1093/mnras/stad1705.

[32] S. Gad-Nasr, K. K. Boddy, M. Kaplinghat, N. J. Outmezguine, and L. Sagunski, *On the late-time evolution of velocity-dependent self-interacting dark matter halos*, 2023. arXiv: 2312.09296 [astro-ph.GA]. [Online]. Available: https://arxiv.org/abs/2312.09296.

Acknowledgements

I would like to express my sincere gratitude to my supervisor, Laura Sagunski, for giving me the opportunity to work on this topic and to be part of her wonderful research group. I would also like to thank Moritz Fischer for his help with my many questions and for kindly agreeing to act as the second examiner and read my thesis. Furthermore, I would like to thank James Gurian and Simon May for their help.
I am also deeply grateful to my friends and fellow students for their support during this time and for their assistance in proofreading this thesis. Finally, I owe special thanks to my family for always being there for me whenever I needed them and for supporting me every step of the way.

Erklärung nach § 39 (15) Prüfungsordnung 2020 für den BAMA-Studiengang Physik

Hiermit erkläre ich, dass ich die Arbeit selbstständig und ohne Benutzung anderer als der angegebenen Quellen und Hilfsmittel verfasst habe. Alle Stellen der Arbeit, die wörtlich oder sinngemäß aus Veröffentlichungen oder aus anderen fremden Texten entnommen wurden, sind von mir als solche kenntlich gemacht worden. Ferner erkläre ich, dass die Arbeit nicht - auch nicht auszugsweise - für eine andere Prüfung verwendet wurde.

Ort, Datum: ..... Unterschrift: .....